IEEE Access
Multidisciplinary | Rapid Review | Open Access Journal

Received 21 September 2023, accepted 5 November 2023, date of publication 8 November 2023,
date of current version 14 November 2023.

*Digital Object Identifier 10.1109/ACCESS.2023.3331224*

RESEARCH ARTICLE

# Dual-Mode Characteristic Based on Miniaturized Metamaterial for Multiband Operation Utilizing Double-Layer Interdigital and Trisection Step-Impedance Techniques

**P. CHOMTONG[1], (Member, IEEE), P. KRACHODNOK[2], (Member, IEEE), C. MAHATTHANAJATUPHAT[3], (Member, IEEE), N. SOMJIT[4,5,6], (Senior Member, IEEE), AND P. AKKARAEKTHALIN[3], (Member, IEEE)**

[1]Department of Teacher Training in Electrical Engineering, Faculty of Technical Education, King Mongkut's University of Technology North Bangkok, Bangkok 10800, Thailand
[2]School of Telecommunication Engineering, Institute of Engineering, Suranaree University of Technology, Nakhon Ratchasima 30000, Thailand
[3]Department of Electrical and Computer Engineering, Faculty of Engineering, King Mongkut's University of Technology North Bangkok, Bangkok 10800, Thailand
[4]School of Electronic and Electrical Engineering, University of Leeds, LS2 9JT Leeds, U.K.
[5]Division of Micro and Nanosystems (MST), KTH Royal Institute of Technology, 114 28 Stockholm, Sweden
[6]Department of Electrical Engineering, Faculty of Engineering, Chiang Mai University, Chiang Mai 50200, Thailand

Corresponding author: P. Krachodnok (priam@sut.ac.th)

The work of P. Chomtong was supported by the King Mongkut's University of Technology North Bangkok under Contract KMUTNB-65-know-31. The work of P. Krachodnok was supported by the Suranaree University of Technology (SUT) Research and Development Fund under Grant IRD7-709-67-12-03. The work of N. Somjit was supported in part by the Engineering and Physical Science Research Council under Grant EP/S016813/1, and in part by the Swedish Research Council (Vetenskapsrådet: VR) under Grant 2021-05842_VR.

**ABSTRACT** This paper presents a dual-mode characteristic for miniaturized metamaterial with a unit cell design based on an interdigital coplanar waveguide (ICPW) combined with trisection step-impedance to enable the three resonant frequency responses of 1.8 GHz, 3.7 GHz, and 5.8 Hz. In addition, the unit cell dimensions can be reduced from $\lambda/2$ to $\lambda/8$ due to the fact that the ICPW technique based on the CPW structure enhances the capacitive load between the transmission line and the side ground, thereby increasing the slow-wave on the transmission line. In addition, the trisection step- impedance will be incorporated and applied to the transmission line and cooperate with the unit cell structure's capacitive load to effectively resonate at the desired frequency location. Moreover, the unit cell structure designed with the method above must be utilized as a double layer in which the structure on both sides is identical. The back structure will property the rod, which will cause the permittivity and permeability to be negative and closer to zero. This property of the proposed material allows for its utilization as a director at its first resonant frequency and as a reflector at the subsequent second and third resonant frequencies. The proposed metamaterial employs FR-4 printed circuit boards with a dielectric constant ($\varepsilon_r$) of 4.4, a substrate thickness of 1.6 mm, a conductor thickness of 0.035 mm, and a loss tangent ($\tan\delta$) of 0.04. The unit cell size is approximately 14 mm$\times$14 mm. The unit cell will then be arranged as a $7 \times 7$ array with an overall dimension of $98 \times 98$ mm$^2$ to evaluate an antenna's performance. An antenna used for testing the proposed unit cell is a dipole antenna that propagates at a single frequency corresponding to the unit cell's resonant frequency. At all resonant frequencies, the impedance matching of the dipole is less than $-10$ dB. At 1.8 GHz, 3.7 GHz, and 5.8 GHz, the dipole antenna gain is 2 dBi, 2.06 dBi, and 1.95 dBi, respectively. Moreover, the dipole antenna's characteristics were simulated using the CST program in conjunction with the unit cell array. Based on the simulation and measurement results, the antenna with the unit cell array exhibits an impedance bandwidth of less than $-10$ dB at frequencies of 1.8, 3.7, and 5.8 GHz. The gains obtained from the simulation results are 5.49 dBi, 8.21 dBi, and 7.87 dBi, while the measurement results show gains of 5.73 dBi, 8.19 dBi, and 7.79 dBi, respectively. The simulated and measured outcomes demonstrate a substantial correspondence.

The associate editor coordinating the review of this manuscript and approving it for publication was Ladislau Matekovits.

**INDEX TERMS** Metamaterial, multi band, ICPW, director, reflector, coplanar waveguide, capacitive load, interdigital.

## I. INTRODUCTION

Various varieties of wireless communication technology have been devised for use in various fields. Therefore, current and future wireless communication devices must be compact, lightweight, sensitive to a broad spectrum of frequencies, and cost-efficient. Antennas serve an essential part in the transmission of data, and research has been performed to continuously improve their efficiency, whether by increasing the gain of the antenna to increase the distance for receiving-transmitting, implementing directional control for antenna propagation, or developing antenna structures that possess smaller and responsive to a broad range of frequencies. In addition to this innovation, one of the contributions to the wireless communication system is the metamaterials [1], [2], [3], [4], [5], [6], [7], [8], [9], [10], [11], [12], [13], [14], [15], [16], [17], [18], [19], [20], [21], which is the design of materials with nonexistent properties, i.e., the material's permittivity ($\varepsilon$) and permeability ($\mu$) are either negative or both negative.

This alters the properties of the material; for instance, if the permittivity is made negative, the material's characteristic will function as a reflection to increase antenna gain more effectively than conventional materials. Additionally, negative permeability enables a material's property to transmit energy from an antenna, which can then be used to direct the protective antenna case [22], [23]. It is possible to categorize metamaterial design into several forms. For instance, a frequency-selective surface (FSS) [24], [25], [26], [27] is a material configuration that allows only the desired frequency range to travel through; all other frequencies are reflected. The electromagnetic band gap (EBG) [28], [29], [30], [31], [32] is a method of material design that can eradicate surface waves when receiving energy from a source and leave only wave propagation, which, if used as a reflector, will result in greater reflection than conventional materials. Magneto dielectric [33], [34] design utilizes the properties of high-frequency circuits and electromagnetic fields to modify the substrate coefficient as a way to accomplish the desired material coefficient. As can be seen, metamaterials appear in a variety of forms. In addition to the above-mentioned metamaterial design, there are numerous studies and research to make the material more efficient, such as designing a multiband metamaterial that can operate in a wide range of frequencies, developing the metamaterial structure smaller than conventional designs, and classifying metamaterial as a double negative.

Previous research showed that the metamaterial, designed to exhibit responsiveness across multiple frequencies, was subjected to testing alongside a multiband antenna. The results indicated that the antenna's gain was significantly enhanced. Nevertheless, the antenna's radiation pattern remains distorted due to its higher mode [35], [36], [37], [38]. Due to the limitations of the design materials, it is challenging to control the variation coefficient over multiple spectra of desired resonant frequencies and to have a compact overall structure suitable for all forms of communication. Therefore, this paper presents a dual-mode characteristic based on miniaturized multiband metamaterial. The metamaterial structure is created from 7 $\times$ 7 unit cells. The interdigital coplanar waveguide (ICPW) [39], [40] technique is combined with trisection step-impedance [41], [42] to generate a unit cell structure that resonates the triple frequency at 1.8 GHz, 3.7 GHz, and 5.8 GHz. The ICPW technique is derived from CPW by incorporating an interdigital structure into the transmission line, which increases the capacitive load at the transmission line's end as a result of the interdigital stage positioned between the transmission line and the side semi-ground. Consequently, the electromagnetic wave on a transmission line will be significantly slowed down or slow wave effect [43], [44], [45], [46], [47], causing the electrical length to differ from the physical length and all resonant frequencies to depart significantly close to zero. Therefore, the physical length must be decreased to restore the resonant frequency to its original frequency, resulting in a reduction in the scale of the structure. The first-order resonance frequency then resonates at the original frequency, whereas the second-order to $N$-order resonance frequencies are shifted away from the original resonance frequency by the capacitive load. It has a strong effect at even mode resonance frequencies (2, 4, 6, 8...$N$) and a weak effect at odd mode resonance frequencies (1, 3, 5, 7...$N$), thereby shifting distinct resonant frequencies. To control the first through third resonance frequencies in order to attain the desired resonance frequency. Utilizing the differential impedance, a trisection step-impedance technique is utilized in the transmission line to govern the transition of the three complementary resonance frequencies with the capacitive load. Consequently, the proposed unit cell is smaller than the conventional design at wavelengths of $\lambda/2$ and regulates up to three resonance frequencies. Upon investigating the permittivity and permeability of the unit cell, it was discovered that the negative permeability characterizes the director at the first resonance frequency, whereas the negative permittivity characterizes the reflector at the second-order and third-order resonance frequencies. Both of the negative values of the resonant frequency are inadequately low. To provide the negative value closer to the double negative value, we will design the rear section with the same unit cell structure as the front section to improve the permittivity and permeability values. It was discovered that the resonance's properties were similar to those of the single-layer structure, with the exception of a more negative coefficient. The present research utilizes FR-4 with a dielectric constant ($\varepsilon_r$) of 4.4, a loss tangent (tan$\delta$) of 0.04, and a substrate height of 1.6 mm. The front and rear coppers thickness are 0.035 millimeters. Consequently, the proposed structure is not entirely double negative, but it is adequate

for increasing the negative value of the coefficient across the resonant frequency range. This indicates that the posterior layer has no effect on the resonant frequency, but is instead characterized by rod [24], which brings both coefficients closer to double negative. In addition, the capacitive load on the rear unit cell structure enhances the capacitive load on the proposed structure, thereby decreasing the size of the unit cell from $\lambda/2$ to $\lambda/8$ in comparison to the conventional design. Due to the design technique, the unit cell is 14 mm $\times$14 mm in dimension and can respond to three resonance frequencies. The unit cell is then arranged into a 7 $\times$ 7 array with a total dimension of 98 mm $\times$ 98 mm. The characteristics of the antenna incorporating the proposed metamaterial will be evaluated using the CST antenna simulator. A comparison will be performed between the simulated values and the actual measurements. The proposed metamaterial possesses properties as a director at the first-order resonance frequency and properties as a reflector at the second-order and third-order resonance frequencies. In the next section of the article, the design concept will be discussed.

## II. DESIGN OF THE DOUBLE LAYER MULTI BAND META MATERIAL UNIT CELL

### A. UNIT CELL DESIGN AND EQUIVALENT CIRCUIT

The metamaterial unit cell design demonstrated in this section consists of a double-layer structure with identical dimensions and appearance on both sides. The rear form possesses rod properties, contributing to near-zero or negative permittivity and permeability when used in conjunction with the front structure, thereby modifying the material properties without distorting the front structure's resonant frequency. The structure of the unit cell depicted in Fig. 1 consists of the front and back layers. Each side of the structure has identical dimensions. It is based on a coplanar waveguide (CPW) comprised of a transmission line with a section of ground plane. The unit cell is designed with a first-order resonant frequency of 1.8 GHz (LTE), while regulating the second-order and third-order resonant frequencies of 3.7 GHz (Wi-MAX) and 5.8 GHz (Wi-Fi), respectively. From the CPW-based unit cell structure, the interdigital technique, also known as Interdigital CPW (ICPW) [40], modifies the capacitance between the transmission line of CPW and the semi-ground, which possesses the characteristics of a capacitive load connection at the terminus of a transmission line. Because of applying the ICPW to the transmission line, the capacitive load value exceeds the typical capacitive load arising from the transmission line, resulting in an extremely slow wave effect on the transmission line. The phenomenon will cause the transmission line's electrical length and physical length to be unequal; the electrical length will increase while the physical length remains constant. As a result, all mode resonance frequencies migrate closer to zero. This is particularly true at the even mode resonant frequencies (2, 4, 6, 8...$N$), whereas the first-order resonance frequency and odd-mode resonance frequencies (1, 3, 5, 7...$N$) will also have a frequency shift

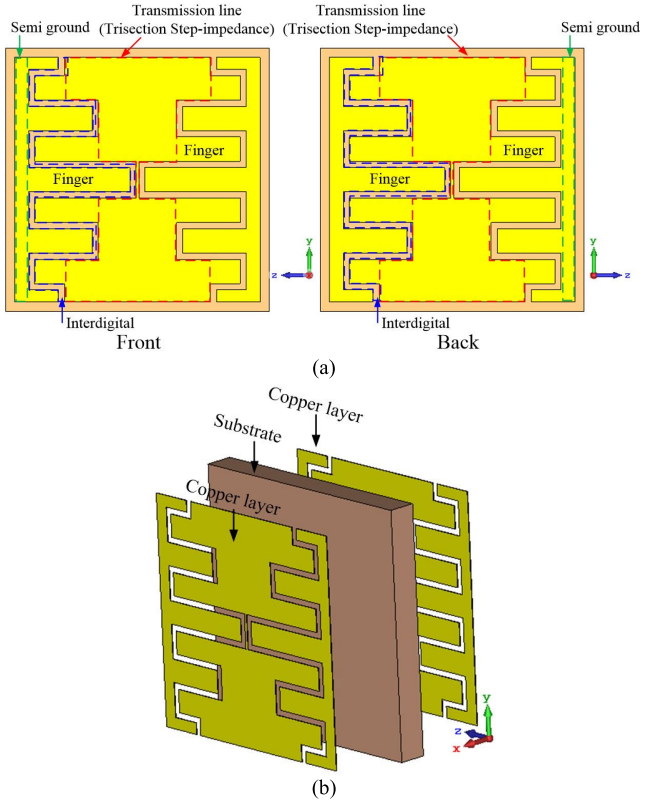


**FIGURE 1.** The proposed structure of the double layer multiband metamaterial unit cell (a) front and back structures of the unit cell (b) material layer of the unit cell.

close to zero, albeit to a less significant degree. To return the first-order resonance frequency to the original frequency, the transmission line's physical length must be shortened until its electrical and physical lengths are identical. The interdigital technique has a very high capacitive value, producing a large slow wave effect that can reduce the overall size of the unit cell structure from $\lambda/2$ to approximately $\lambda/8$. Increasing or decreasing the capacitive load of the ICPW technique on the structure of the unit cell is dependent on the length, width, number of digits, and distance between the transmission line and semi-ground in the interdigital region. Although the first-order resonance frequency can be shifted back to its original resonance frequency range, the second-order and third-order resonance frequencies shift away from zero without resonating at the desired frequency. The capacitive load can regulate the second-order resonance frequency to accomplish the requisite resonance with minimal effect on the first-order resonance frequency. However, the capacitance load at third-order resonance frequency is less affected than at second-order resonance frequency, making it challenging to control the three resonances across the frequency spectrum by applying only the capacitive load method. Therefore, in order to control three resonance frequencies, the transmission line's impedances of various dimensions must be used to control the resonance of the three frequencies within the desired frequency range. For second-order and third-order resonance

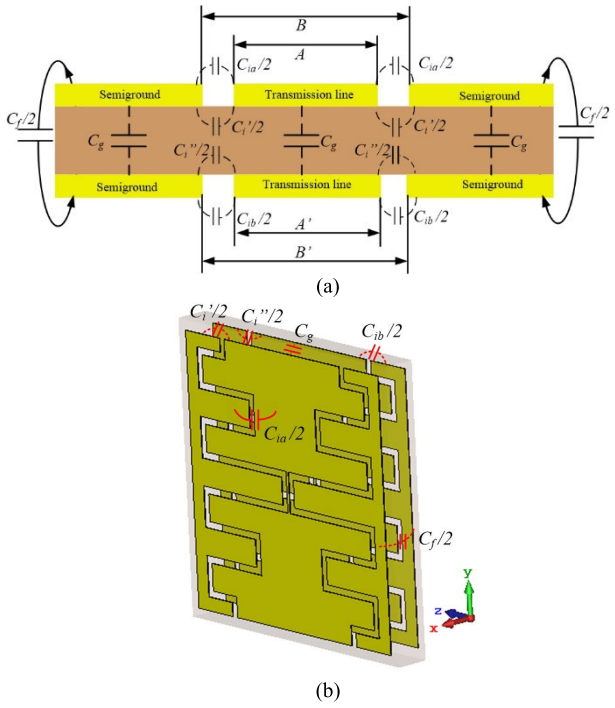


**FIGURE 2.** The capacitive coupling of the proposed unit cell in (a) cross section and (b) 3D dimensionl.

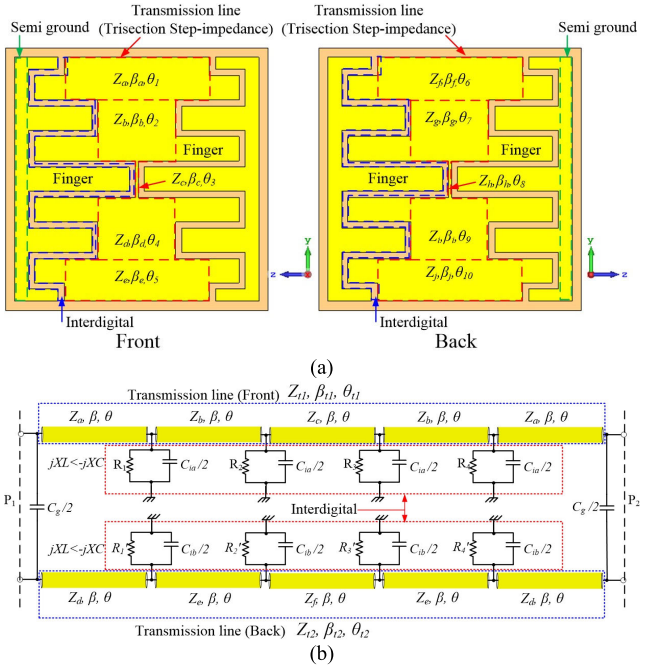


**FIGURE 3.** The configuration of the proposed unit cell and parameters (a) Trisection transmission line of front and back layer and (b) equivalent circuit of the proposed unit cell.

control, the transmission line structure is utilized in conjunction with the trisection step-impedance methodology [41], [42]. The trisection step impedance approach involves the division of the transmission line into three distinct sections. The impedance ratio of each component of the transmission line will be evaluated in comparison to the parameter $K$. The $K$ value will be further examined in the circuit analysis of Fig. 3 as presented in (3) and (4). The independent control of the second and third resonant frequencies, while maintaining the first frequency constant, is achieved by the manipulation of the impedance ratio of each element. By modifying the three impedances in accordance with the capacitive load on the structure, it is possible to precisely control the second-order and third-order resonant frequencies, while there is no resonance shift for the first-order resonance frequency. The front and back structures of the trisection step-impedance applied to the transmission line are symmetrical.

Upon analyzing the capacitance generated on the unit cell structure, it was discovered that in addition to the capacitive load connected at the transmission line's end due to the interdigital phase, there was also a capacitance generated on the unit cell structure, as depicted in Fig. 2 [43], [44], [45], [46]. According to the Fig. 2(a), the capacitance influencing the desired resonance frequency range can be separated into $C_{ia}$ and $C_{ib}$, which represent the capacitive load between the transmission line and the semi-ground of the interdigital region in the front as well as the rear of the structure, respectively. This capacitance is characterized by a capacitive load connected to the transmission line's end that produces the previously described effect. $C_i'$ and $C_i$" are the capacitive values that occur anteriorly and posteriorly on the unit cell structure between the transmission line and semi-ground within the substrate as depicted in Fig. 2(b), which have a negligible effect on the structure and frequency resonance. $C_f$ is the capacitance between the upper and lower semi-grounds, which has a negligible impact on the structure and frequency resonance. $C_g$ is the capacitance formed between semi-ground to semi-ground and transmission line to transmission line in the structures of the front and rear unit cells. Because it is a capacitive load connected to the transmission line's termination, it influences the resonant frequency just like $C_{ia}$ and $C_{ib}$. However, increasing or decreasing the capacitive load for controlling the resonant frequency is accomplished by modulating the $C_{ia}$ and $C_{ib}$ values within the interdigital range, as it is simpler to modify than $C_g$ [39], [40]. Fig. 3 depicts the configuration of the proposed unit cell. By analyzing the structure of the unit cell, it is possible to determine that the transmission line utilizing the trisection step-impedance technique has a symmetrical structure with front and rear dimensions that are identical. Each segment includes the intrinsic impedance ($Z$), the propagation constant ($\beta$), and the electrical length ($\theta$). The impedance is divided into $Z_a$, $Z_b$, and $Z_c$ for transmission line impedance on the front structure and $Z_d$, $Z_e$, and $Z_f$ for transmission line impedance on the rear structure. Fig. 3(a) illustrates that where $Z_a = Z_d$, $Z_b = Z_e$, and $Z_c = Z_f$, the total impedance of the transmission line on the front and rear structures are $Z_{t1}$ and $Z_{t2}$, the total propagation constant of the front and rear conductors are $\beta_t$ and $\beta_t'$, and the total electrical length of the front and rear conductors is $\theta_t$ and $\theta_t'$. Moreover, within the

equivalence circuit depicted in Fig. 3(b), each segment of the front and rear transmission lines are connected by a capacitive load generated in the interdigital segment, denoted by $C_{ia}$ and $C_{ib}$. The loss in transmission lines of $R_1$-$R_4$ and $R_1$'-$R_4'$ occur in the interdigital section, which has a high capacitance, thus $jX_L < -jX_C$. In addition, the capacitive load $C_g$ between the front and rear regions of the transmission line is connected, resulting in a significant increase in the capacitive load of the structure, causing effectively slow waves as well. Applying the ICPW technique, the capacity of the unit cell can be drastically reduced from the structure of the unit cell. The total capacitance of the structure ($C_{ICPW}$) can be calculated using (1) [40].

$$C_{ICPW} = C_{ia} + C_{ib} + C_g + C_i' + C_i^{"} + C_f \tag{1}$$

When

$$C_{ia} = \frac{(\varepsilon_r + 1)}{L_t} L_f\,(\varepsilon_r + 1)\,(0.1\,(n-3) + 0.11) = C_{ib},$$

$$C_i' = \frac{\varepsilon_0 \varepsilon_r}{\pi} \ln\left[\cot h\left(\frac{\pi}{4}\frac{B}{h}\right)\right] + 0.65\, c_f \left(\frac{0.02}{B/h} + 1 - \frac{1}{\varepsilon_0^2}\right) = C_i"$$

$$C_g = \varepsilon_0 \varepsilon_r \frac{A}{h},$$

$$C_f = \frac{\sqrt{\varepsilon_r}}{(C_{zt}) - (C_g)}.$$

From (1), $L_t$ is the total length of the interdigital section, $L_f$ is the length of the capacitive finger section, $n$ is the number of fingers, $A$ and $A'$ are the transmission line width, $B$ and $B'$ are the transmission line width to semi-ground, $h$ is the height of the substrate, and $C_{Zt}$ is the capacitance of semi ground. According to the structure of the unit cell, the values of $C_i'$, $C_i$", and $C_f$ have a negligible effect on the resonant frequency. Equation (2) represents the entire capacitance of the unit cell structure. On the unit cell structure, the capacitive load at the transmission line's end is high, exceeding the normal capacitive load at the transmission line's end [44], [45], [46]. Consequently, it generates a slower wave effect.

$$C_{ICPW} = C_{ia} + C_{ib} + C_g \tag{2}$$

In the transmission line segment utilizing the trisection step-impedance technique, the impedance is segmented into three segments that correspond to the first-order to third-order resonance frequencies. To accomplish the intended resonance frequency, the difference between the impedances is used to control the resonant frequency. Equation (3) [42] can be utilized to determine the electrical length of each transmission line segment, where the electrical length of each transmission line segment is denoted by $\theta$. To derive the electrical lengths at first-order ($f_1$), second-order ($f_2$), and third-order ($f_3$) resonant frequencies, one determines the electrical lengths at first to third resonant frequencies and assigns them the values $\theta_1$, $\theta_2$, and $\theta_3$ respectively. The ratio between the impedances of the transmission line is $K_1 = Z_a/Z_b = Z_d/Z_e$, and $K_2 = Z_b/Z_c = Z_e/Z_f$.

$$\theta_1 = \tan^{-1}\sqrt{\frac{K_1 K_2}{1 + K_1 + K_2}},$$

$$\theta_2 = \tan^{-1}\sqrt{\frac{1 + K_1 + K_1 K_2}{K_2}},\ \theta_3 = \pi/2. \tag{3}$$

From (3), the relationship between the electric length in the resonant frequency range and the required resonant frequency can be obtained according to (4) [41], [42].

$$\frac{f_2}{f_1} = \frac{\theta_2}{\theta_1} = \frac{\tan^{-1}\sqrt{\frac{1+K_1+K_1K_2}{K_2}}}{\tan^{-1}\sqrt{\frac{K_1K_2}{K_1+K_2+1}}},$$

$$\frac{f_3}{f_1} = \frac{\theta_3}{\theta_1} = \frac{\pi - \tan^{-1}\sqrt{\frac{K_1K_2}{1+K_1+K_2}}}{\tan^{-1}\sqrt{\frac{K_1K_2}{K_1+K_2+1}}}. \tag{4}$$

The total impedance can be derived from the relationship between the impedance ratio and the internal resonant frequency of the trisection step-impedance transmission line using (5) when $Z_{t1} = Z_{t2}$, where $Z_{t1}$, $Z_{t2}$ are the total impedances of trisection step-impedance transmission line in front and back structure, respectively.

$$Z_{t1} = \frac{1}{Y_{t1}} = jZ_a \frac{\left(Z_cZ_b + Z_b^2 + Z_cZ_a\right)\tan\theta - Z_a\tan^3\theta}{Z_bZ_a - \left(Z_cZ_b + Z_b^2 + Z_cZ_a\right)\tan^2\theta} = Z_{t2} \tag{5}$$

From the double-layer unit cell structure utilizing the ICPW technique, which uses a trisection step-impedance transmission line to connect the capacitive load with an interdigital technique, the total electrical length at the resonant frequency can be calculated using (6), where $\theta_{a1}$, $\theta_{a2}$, and $\theta_{a3}$ are the electrical lengths at the first, second, and third order resonance frequencies, respectively.

$$\theta_{a1} = 2\tan^{-1}\left(\frac{1}{\pi f_1 Z_{t1} C_{ICPW}}\right),$$

$$\theta_{a2} = 2\pi - 2\tan^{-1}\left(\pi f_2 Z_{t1} C_{ICPW}\right),$$

$$\theta_{a3} = 2\tan^{-1}\left(\frac{1}{\pi f_3 Z_{t1} C_{ICPW}}\right). \tag{6}$$

According to (6), the capacitive load and transmission line's total impedance have a significant effect at the second-order resonance frequency but a negligible effect at the first-order resonance and third-order resonance frequencies. Therefore, the transmission line impedance can be used to control the second-order resonant frequency coupled with the capacitive load, allowing the unit cell structure to respond to multiple frequencies and substantially reduce its dimensions. The unit cell's parameter structure is depicted in Fig. 4 and summarized in Table 1. The simulation of CST software will be used to evaluate the unit cell. To investigate the proposed unit cell characteristic, the $Z$-axis boundary condition is set to the direction that transmits the electromagnetic wave to the unit

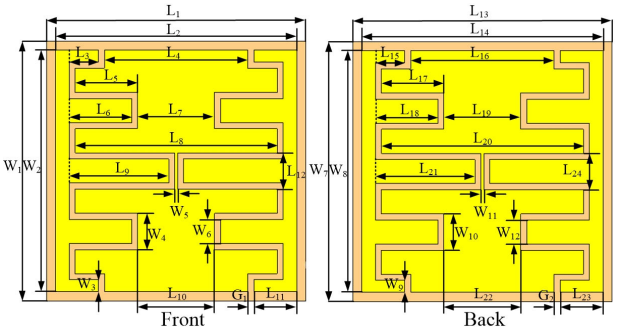


**FIGURE 4.** The proposed unit cell configuration and parameters.

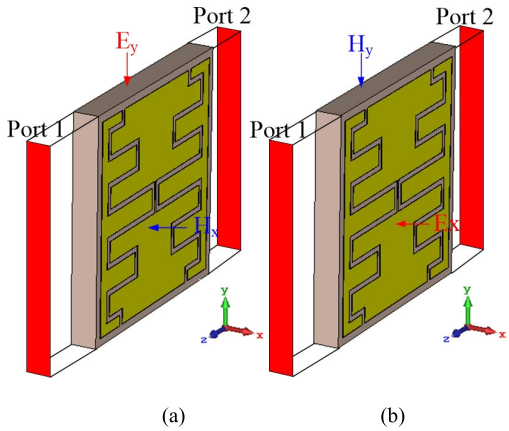


**FIGURE 5.** Simulation setup of the wave transmission with (a) E-field on the Y-axis and H-field on the X-axis and (b) E-field on the X-axis and H-field on the Y-axis.

**TABLE 1.** Parameters of unit cell.

| Dimensions of unit cell [a] | |
|---|---|
| $L_1 = L_{13}$ =14.00 mm. | $L_{12} = L_{24}$ = 1.30 mm. |
| $L_2 = L_{14}$ = 13.02 mm. | $W_1 = W_7$ = 14.00 mm. |
| $L_3 = L_{15}$ = 1.58 mm. | $W_2 = W_8$ = 13.02 mm. |
| $L_4 = L_{16}$ = 7.75 mm. | $W_3 = W_9$ = 0.65 mm. |
| $L_5 = L_6 = L_{17} = L_{18}$ = 3.37 mm. | $W_4 = W_{10}$ = 1.95 mm. |
| $L_7 = L_{10} = L_{19} = L_{22}$ = 4.15 mm. | $W_5 = W_{11}$ = 0.15 mm. |
| $L_8 = L_{20}$ = 10.91 mm. | $W_6 = W_{12}$ =1.30 mm. |
| $L_9 = L_{21}$ = 5.37 mm. | $G_1 = G_2$ = 0.32 mm. |
| $L_{11} = L_{23}$ = 2.30 mm. | $h$ = 1.6 mm. |

cell, and the $X$- and $Y$-axes boundary conditions are set to the electrical field or magnetic field. Consider the $E$-field axis to be the axis along which a dipole antenna with a unit cell array is positioned.

Fig. 5 displays the functioning of the $E$- and $H$-fields on the $X$- and $Y$-axes. Fig. 5(a) depicts the $E$-field along the $Y$-axis and the $H$-field along the $X$-axis. As indicated in Fig. 5(b), the $E$-field is defined along the $X$-axis and the $H$-field along the $Y$-axis. During the test, it is observed that incoming wave power is transmitted along the $Z$-axis into the unit cell structure via port 1, the transmission line, and port 2.

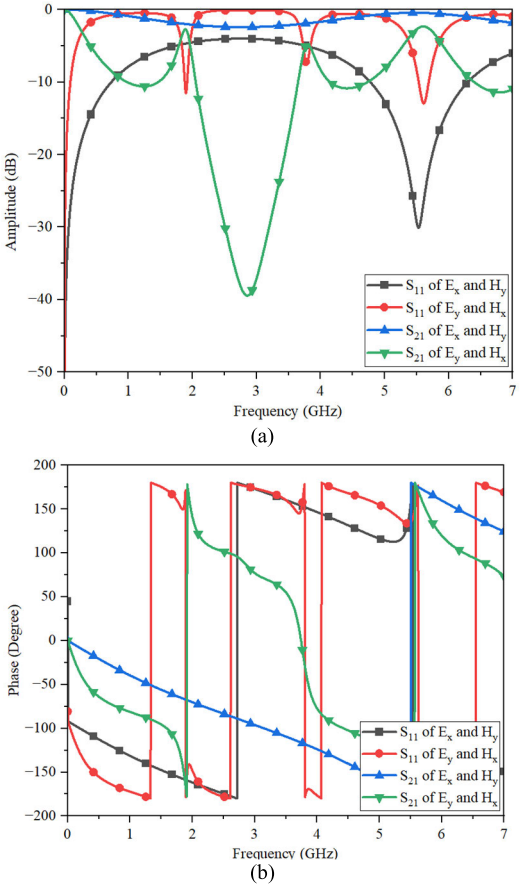


**FIGURE 6.** Comparison of $S_{11}$ and $S_{21}$ simulation results as altering E- and H-fields along the *X*- or *Y*-axis with (a) amplitude and (b) phase.

Comparing this power transmission to the equivalence circuit depicted in Fig. 3, it is evident that the unit cell's energy transfer characteristics are identical. The $S_{11}$ and $S_{21}$ simulation results are evaluated and compared as depicted in Fig. 6. When the $E$-field is aligned along the $Y$-axis and the $H$-field is aligned along the $X$-axis as corresponding in Fig. 5a, the unit cell can respond effectively to all three resonance frequencies. The transmission coefficient $S_{21}$ and the reflection coefficient $S_{11}$ occur precisely in the intended resonant frequency range, i.e., the first-order resonant frequency range at 1.8 GHz, the second-order resonant frequency at 3.7 GHz, and the third-order resonant frequency at 5.8 GHz as shown in Fig. 6a. However, in the case where the $E$-field is oriented parallel to the $X$-axis and the $H$-field is oriented parallel to the $Y$-axis, as depicted in Fig. 5b, it has been observed that the frequency response remains within the pass band across the range of 0 to 7 GHz as shown in Fig. 6a. Nevertheless, this configuration exhibits a significant insertion loss and a low return loss, thereby limiting its ability to effectively manipulate the resonant frequency according to desired specifications. The observation of Fig. 6b reveals the presence of a phase shift transitioning from a positive to a negative value at the resonant frequency. The metamaterial exhibits alterations in its permittivity and permeability characteristics

at distinct resonance frequencies when the $E$-field is oriented along the $Y$-axis and the $H$-field is oriented along the $X$-axis. Conversely, there is negligible phase shift observed when the $E$-field is aligned along the $X$-axis and the $H$-field is aligned along the $Y$-axis.

### B. PARAMETRIC STUDY

For controlling all three resonance frequencies, it can be seen that the finger in the interdigital range, as represented by the parameters $L_6$ and $W_4$, will influence the shift of all resonant frequencies, particularly at the second-order resonance frequency, as depicted in Fig. 7. It is indicated that the resonance shift can be observed across all frequency ranges. First-order and third-order resonant frequencies, which are in odd mode, have less impact than second-order resonance frequency, which is in even mode. This permits the second-order resonant frequency to adjust the resonant frequency further because the capacitive load generated within the interdigital range has a substantial effect on the resonant frequency. This corresponds to the relationship depicted in (6) between the resonant frequency and the capacitance of the unit cell. In addition to applying a capacitive load to the frequency shift, there exists a control technique in the transmission line section for regulating the resonance at all frequencies to obtain resonance within the specified frequency range.

On the transmission line, the trisection step-impedance technique is applied to control the resonant frequencies. As depicted in Fig. 8, the parameters $L_4$, $L_7$, and $W_5$, which are used to calculate the impedance ratio of $Z_1$-$Z_3$ to control the resonant frequency, will be determined by the structure of the unit cell. The difference between the three impedances governs the resonance at all three frequencies, as demonstrated. It also influences the resonant frequency shift in the second-order resonant frequency range to a significant degree. The first-order resonant frequency exerts a negligible influence, resulting in a smaller frequency shift than the second-order resonant frequency. Third-order resonance frequency is also affected by frequency shifts, although to a lesser extent than second-order resonance frequency. According to Fig. 8, this indicates that both capacitive and trisection step-impedance values have a significant effect on the second-order resonant frequency. When the ratio of impedances within the cable is altered, the first-order and third-order frequencies experience a smaller frequency shift. Adjusting the capacitive load from the finger and the ratio between the internal impedances of the conductor will therefore reduce the size of the unit cell structure to approximately $\lambda/8$ and precisely control the resonant frequency.

When simulating the ICPW unit cell structure, the unit cell's front and back must be structured in the same direction, with the $E$-field along the $Y$-axis and the $H$-field along the $X$-axis. If the front and back structures are misaligned, the frequency resonance cannot be achieved due to the modification of the equivalence structure. Similarly, if the ICPW of the unit cell structure is arranged horizontally along the $X$-axis, undesirable resonances will occur due to cross-polarization,

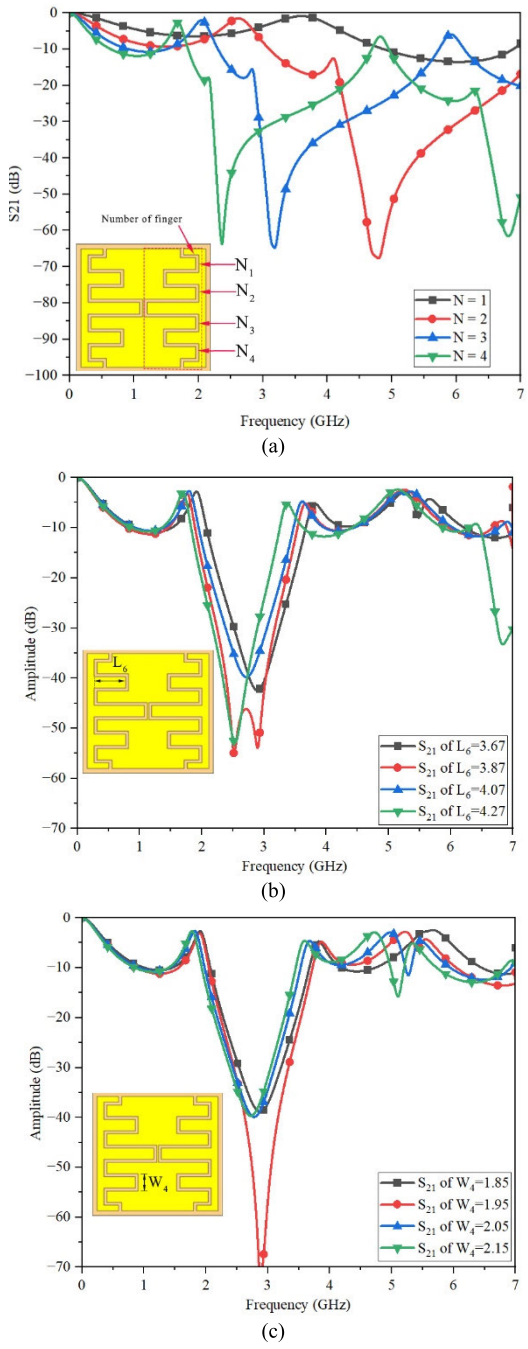


**FIGURE 7.** The effect evaluation of the interdigital finger: (a) number of finger ($N$), (b) finger length ($L_6$), and (c) finger width ($W_4$).

eliminating energy transmission through the transmission line. The unit cell structure's resonance test was performed in all three frequency bands. As illustrated in Fig. 9, the ICPW structure was simulated as a single-layer structure and compared to the double-layer structure. It was found that the first-order to third-order resonance was the same, and when simulating the work to test the permittivity and permeability shown in Fig. 10, the single layer structure had negative permittivity at 2.79GHz – 3.68 GHz and negative permeability at 2.10 GHz – 2.33 GHz. In the double-layer

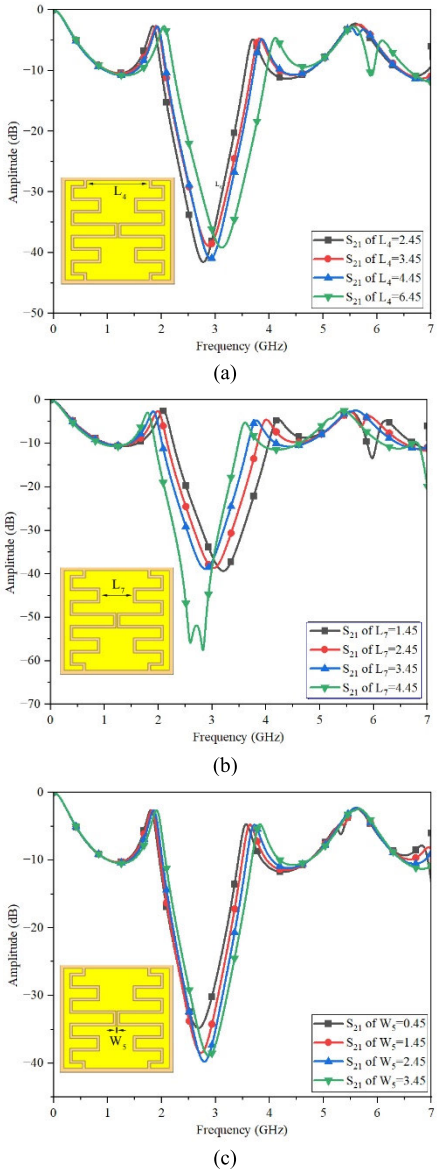


**FIGURE 8.** The effect evaluation of transmission line using the trisection step impedance technique when modifying the parameters of (a) $L_4$, (b) $L_7$, and (c) $W_5$.

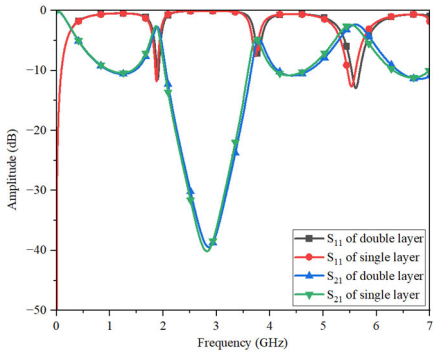


**FIGURE 9.** Comparison $|S_{11}|$ and $|S_{21}|$ simulation result between a single-layer and a double-layer of unit cells.

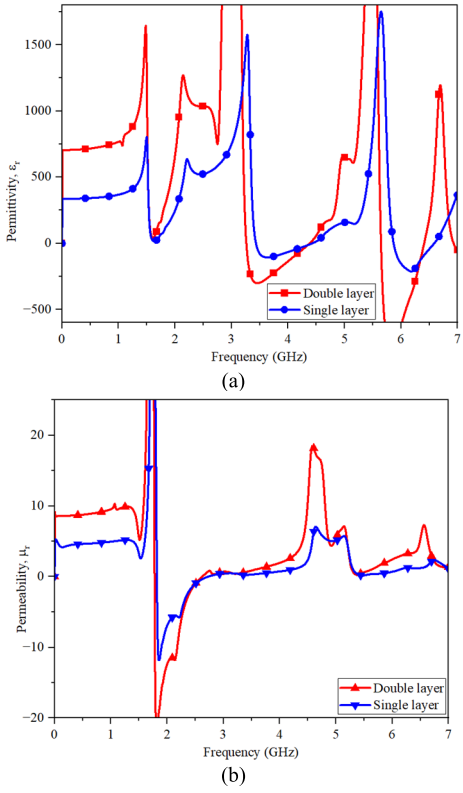


**FIGURE 10.** Comparing the simulation results between single- and double-layer unit cells of (a) permittivity ($\varepsilon$) and (b) permeability ($\mu$).

structure, permittivity was negative in two frequency ranges: 2.68 GHz – 3.85 GHz and 5.21 GHz –5.95 GHz, whereas permeability was negative in 1.69 GHz – 2.6 GHz.

Figs. 9 and 10 show that the single-layer and double-layer structures have the same first-order to third-order resonance frequencies, but the permittivity and permeability coefficients are substantially distinct at first-, second- and third-order resonance frequencies. At the first-, second- and third-order resonance frequencies, permittivity and permeability coefficients of the double layer structure approach zero and increasingly negative values. From these findings, the rear structure improves permittivity and permeability approaching zero or negative. Thus, the unit cell structure has rod [24] features without affecting the resonance characteristics of the appropriate frequency range. The function of the rod is to improve the coefficients of permittivity and permeability of the unit cell so that they approach zero and are both negative. In this instance, however, the resonance frequencies. This indicates that the thickness of the rear copper material, which is only 0.035 mm, is a significant material limitation that causes the coefficient of permittivity and permeability to be close to zero or both negative to some degree. According to the structural properties of the ICPW double-layer unit cell, the transmission of electromagnetic waves at the first resonant frequency is excellent because the permeability value at this frequency is negative. As a result of negative permittivity values, the proposed unit cell effectively reveals the reflector characteristic at second-order and third-order resonance

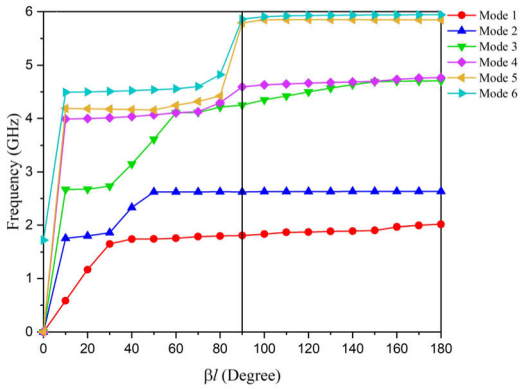


**FIGURE 11.** The simulation results of the unit cell's dispersion diagram.

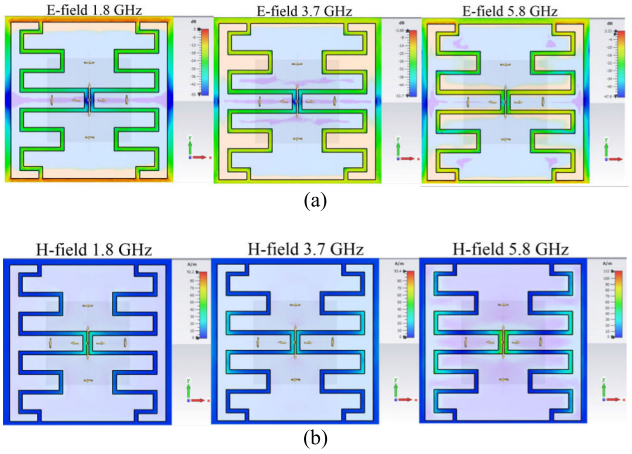


**FIGURE 12.** The simulation results of electric and magnetic fields on the proposed unit cell structures at 1.8 GHz, 3.7 GHz, and 5.8 GHz (a) E-field and (b) H-field.

frequencies with superior reflection properties in comparison to conventional materials. Therefore, the metamaterial characteristics can be explained by considering the permittivity and permeability shown in Fig. 10. Based on the characterization shown in Fig. 10, it has been observed that materials exhibiting negative permittivity properties possess a notable capacity for effectively reflecting waves. Conversely, materials exhibiting negative or almost zero permeability properties demonstrate favorable transmission of energy capabilities. The proposed research has been primarily focused on the examination of the characteristics that manifest within the structure of the proposed unit cell.

The dispersion diagram of the proposed unit cell is illustrated in Fig. 11. The observation indicates that separation appears in the 1.8 GHz frequency range, leading to the absence of surface current within this specific region, hence creating a gap between Mode 1 and Mode 2. Nevertheless, while considering the frequency range of 1.8 GHz, it is evident from Fig. 10 that the metamaterial under investigation exhibits a negative permeability, while the permittivity tends towards zero. Consequently, the quantity of waves has the capability to propagate outward from the metamaterial and undergo reflection upon interaction with the metamaterial. However, while operating at this specific frequency, the majority of the electromagnetic wave is transmitted through the proposed metamaterial due to the elimination of energy loss caused by surface current. Hence, the dissipated energy resulting from surface current is transformed into potential energy inside the unit cell. Subsequently, the energy that has been stored inside the unit cell is discharged, manifesting as an electromagnetic wave with frequencies within the range of 1.8 GHz.

In the frequency range of 3.7 to 5.8, it is seen that there is a lack of separation between Mode 3 and Mode 4, as well as between Mode 5 and Mode 6. Therefore, this absence of separation leads to the generation of surface currents that circulate over the surface. Consequently, a portion of the energy is dissipated at the surface. Nevertheless, throughout the frequency ranges of 3.7 GHz and 5.8 GHz, the metamaterial under consideration exhibits a permeability that is in close proximity to zero, and the permittivity assumes a negative value. Accordingly, the incident energy propagated by the dipole antenna will be concentrated inside the unit cell. The energy that has been collected is then reflected outward. The waves that are reflected from the proposed unit cell will exhibit a state of phase coherence with the waves emitted by the dipole antenna. In particular, the metamaterial including a dipole antenna has a greater aggregate energy output compared to a conventional reflector equipped with an antenna. The congruity between the results derived from the dispersion diagram shown in Fig. 11 and the characteristics of the metamaterial illustrated in Fig. 10 is evident.

Figs. 12 depicts the wave propagation simulation results of electric and magnetic fields on the front and rear unit cell structures when the $E$-fields are aligned along the $Y$-axis and the $H$-fields are aligned along the $X$-axis. At the first resonant frequency, it was discovered that a large $E$-field is generated on the transmission line structure and in the interdigital region, with the highest field density in the unit cell gap. This indicates that at this resonant frequency, it is produced by the transmission line structure and capacitive values of the interdigital region. For the second-order resonant frequency, there is a significant amount of $E$-field strength in the interdigital region and a small amount on the transmission line because, at this frequency, the resonance is controlled by capacitive values, which is the primary effect, and the step-impedance technique applied to the transmission line. In the region of interdigital and unit cell structure, electric field strengths are evident for third-order resonant frequency. This indicates that this third-order resonant frequency is affected by the unit cell's capacitance. Based on the preceding description, it was determined that the unit cell can respond to three resonant frequencies: 1.8 GHz, 3.7 GHz, and 5.8 GHz, with electromagnetic wave transmission characteristics occurring most effectively at the first resonant frequency range. In addition, at second-order and third-order resonant frequencies, it has significant reflection properties that surpass those of a typical

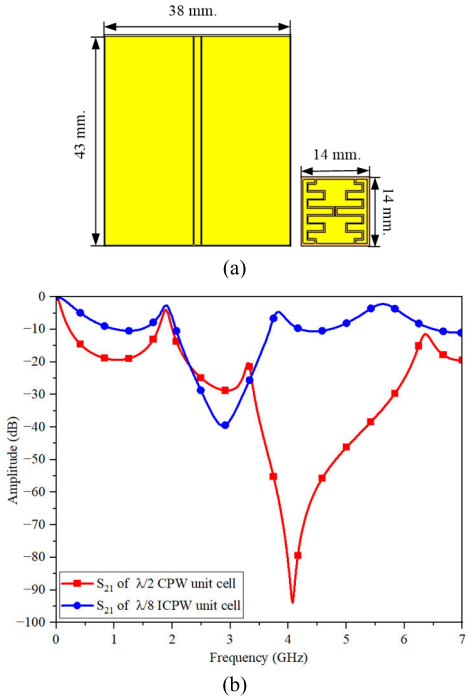


**FIGURE 13. Comparison between the proposed double layer ICPW unit cell and conventional CPW unit cell with (a) the physical dimension and (b) the $|S_{21}|$ simulation results.**

material reflector. After the unit cell design achieves resonance and possesses the desired permittivity and permeability properties, the ICPW unit cell designed at the first resonance frequency of 1.8 GHz has a dimension of $\lambda/8$. As shown in Fig. 13(a), the dimension disparity between the proposed unit cell and a conventional CPW of size $\lambda/2$ is substantial. Fig. 13(b) demonstrates that, for the second-order and third-order resonance frequencies, the typical CPW structure was unable to achieve the resonance frequencies as required. In the next section, the designed unit cell is arranged into an array and its transmittance and reflection properties are evaluated using three single-frequency dipole antennas with the identical resonant frequency as the unit cell.

## III. DESIGN OF ARRAY DOUBLE LAYER MULTI BAND META MATERIAL UNIT CELL WITH ANTENNA

After designing the unit cell derived from the design of the previous section, the connection between the unit cells will be analyzed to determine the frequency distortion, as depicted in Figs. 14. Fig. 14(a) depicts the structure of the interconnection between the two proposed unit cells. It has been discovered that the gap between two unit cells is responsible for the production of $C_a$ capacitance. The capacitance has an effect on the first, second, and third resonant frequencies because it is the capacitive load that is connected to the transmission line's end in the same manner as the ICPW approach. Consequently, this parameter must be regarded and analyzed in (7). It can be seen from (7) that the value of $C_a$ has an effect on all resonant frequencies, with a particularly large effect on second-order resonance frequency. Where $C_a$ is the capacitive load between unit cell connections, $a$ is the width of a unit cell, $W'$ is the width of two unit cells, and $g$ is the gap between unit cells. The simulated results to test the effect of unit cell coupling showed that the $C_a$ values affected all frequency shifts. From the proposed unit cell interconnection structure, there is a very low capacitive value between the gap of the unit cells, thus the proposed unit cell can maintain the original resonant frequency range within the required resonant frequency range. In general, The distance or gap between unit cells is absolutely unaffected by electric and magnetic fields at the resonant frequency must be greater than $0.7h$ when $h$ is the substrate height. In order to reduce the overall size of the connected unit cell smaller, the unit cell gap was designed to be lower than $0.7h$. As a consequence, the induction and coupling effect of magnetic and electric fields on the unit cell gap area has still remained very little effect and it does not significantly affect the resonant frequency range shift. Then, the permittivity and permeability of the proposed unit cells with a single layer and double layer will be analyzed and compared, as shown in Figs. 14 (b) and (c). The permittivity and permeability between the single layer and double layer of the proposed unit cell have not significantly altered the resonant frequency. It appears that the $C_a$ has a negligible effect on the resonance.

$$\begin{aligned}
\theta_{a1} &= 2\tan^{-1}\left(\frac{1}{\pi f_1 Z_{t1}(C_{ICPW}+C_a)}\right),\\
\theta_{a2} &= 2\pi - 2\tan^{-1}\left(\pi f_2 Z_{t1}(C_{ICPW}+C_a)\right),\\
\theta_{a3} &= 2\tan^{-1}\left(\frac{1}{\pi f_3 Z_{t1}(C_{ICPW}+C_a)}\right)
\end{aligned} \tag{7}$$

When

$$C_a = \frac{W'\varepsilon_0(1+\varepsilon_r)}{\pi}\cosh^{-1}\left(\frac{a}{g}\right).$$

Next, the unit cell will be arranged as a $7\times 7$ unit cell array as shown in Fig. 15. The $7\times 7$ unit cell array structure maintains resonant frequency responses of 1.8 GHz, 3.7 GHz, and 5.8 GHz, which is consistent with the previously described $C_a$ value-based coupling effect analysis. The objective of this study is to analyze the frequency response characteristics by employing an identical metamaterial in combination with a basic dipole antenna to obtain the required qualifications and achieve optimal efficiency. However, the implementation of tests on the metamaterial in conjunction with a multiband antenna has the potential to impact the radiation pattern. The presence of higher modes in the multiband antenna can lead to distortion of the radiation pattern, particularly at high frequencies. Consequently, the efficiency of wave reflection is diminished in comparison to its initial state, thereby impeding the accurate determination of the accurate efficiency of the metamaterial [35], [36], [37], [38]. In addition, the $7\times 7$ unit cell array structure was evaluated using a single frequency dipole antenna with impedance matching below $-10$ dB at identical resonant frequencies as the proposed unit cell. The gain was 2.0 dBi, 2.06 dBi, and 1.95 dBi, respectively, with omnidirectional propagation.

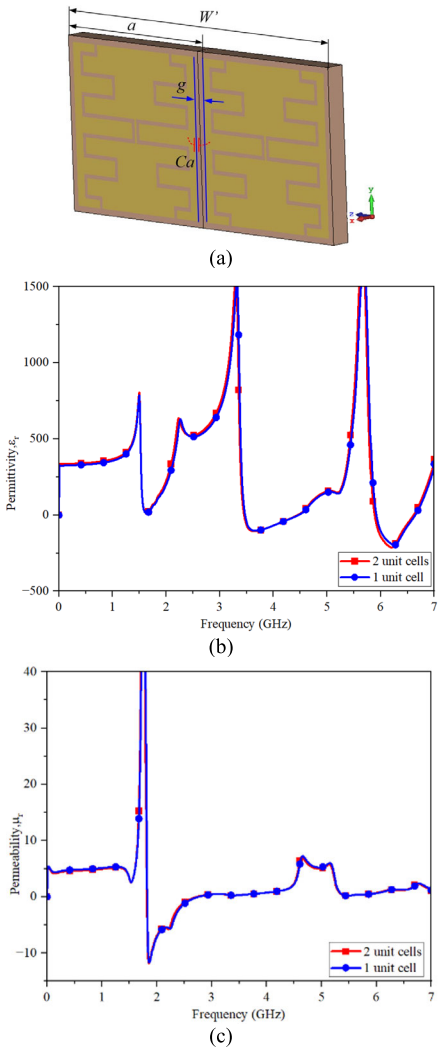


**FIGURE 14.** The coupling effect between the proposed unit cell. (a) structure, (b) permittivity, and (c) permeability .

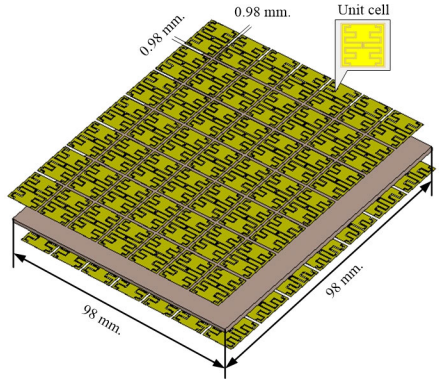


**FIGURE 15.** 7 × 7-unit cell array structure of the proposed metamaterial.

Fig. 16 depicts the structure of the tested dipole antenna, and Table 2 lists its parameters. The tested dipole antenna consists of a copper tube connected to a low-loss cable and a balun circuit that transforms the impedance between the antenna and the cable. To simulate the characteristics of the antenna with the proposed unit cell array, a dipole antenna

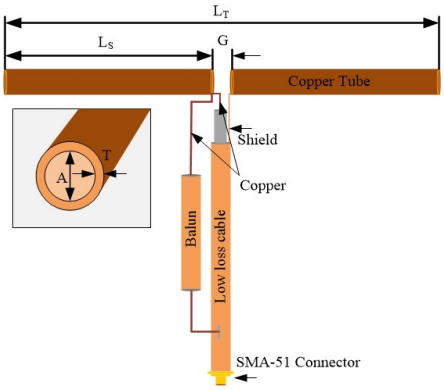


**FIGURE 16.** Dipole antenna configuration.

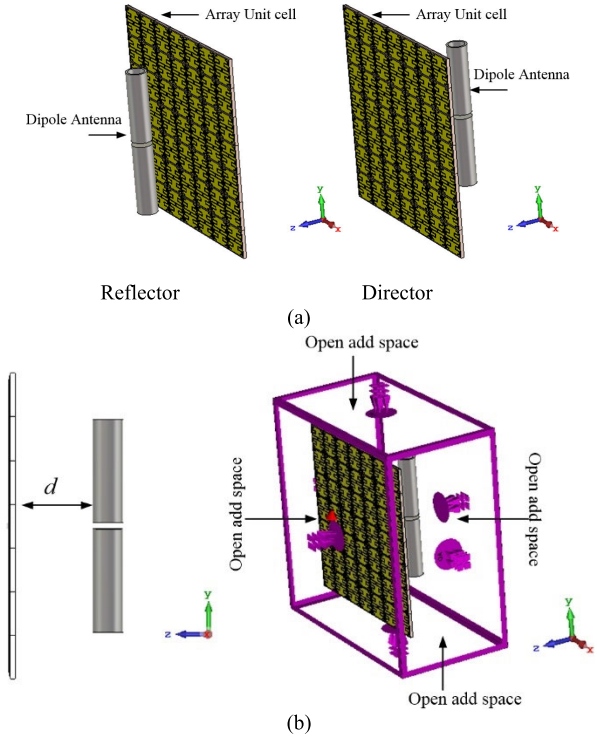


**FIGURE 17.** The installation of proposed unit cell array with dipole antenna: (a). director or reflector mode and (b) bound condition.

was placed behind the unit cell array to examine the transmittance at the first resonant frequency, and a dipole antenna was placed in front of the unit cell array to verify the reflection property for the second-order and third-order resonance frequencies, as illustrated in Fig. 17(a). Since the antenna must be in-phase with the unit cell array, the distance between the dipole antenna and the unit cell array is a significant factor that depends on the size of the unit cell structure; if the unit cell is smaller than $\lambda/2$, the distance ($d$) between the dipole antenna will be less than $\lambda/4$ [22]. At the first, second, and third resonant frequencies, the distance ($d$) between the antenna and the unit cell array was 15.3 mm, 12.4 mm, and 7.6 mm, respectively. As depicted in Fig. 17(b), the boundary conditions of the $X$-, $Y$-, and $Z$-axes are set to the open add

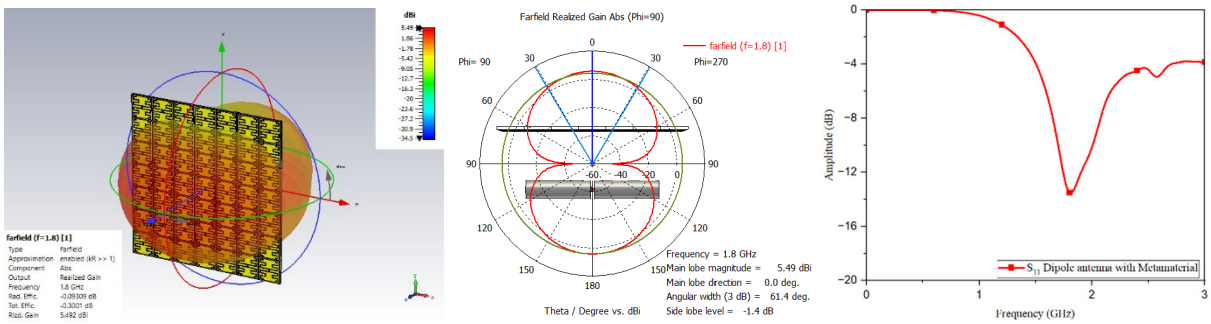


(a)

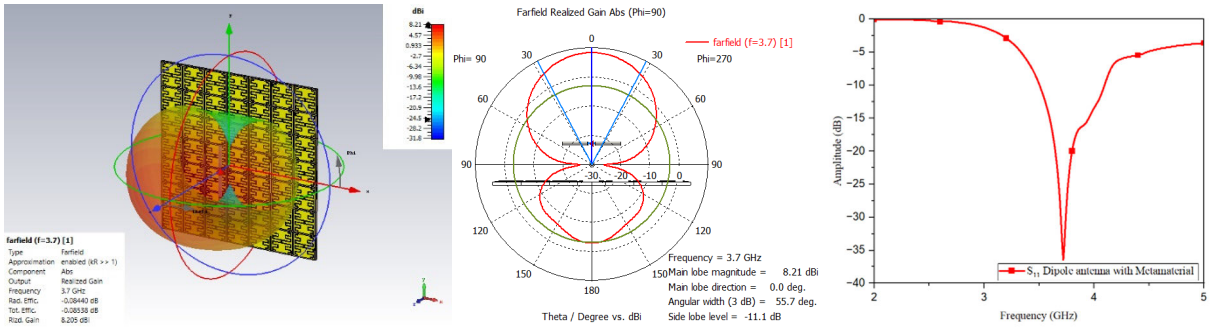


(b)

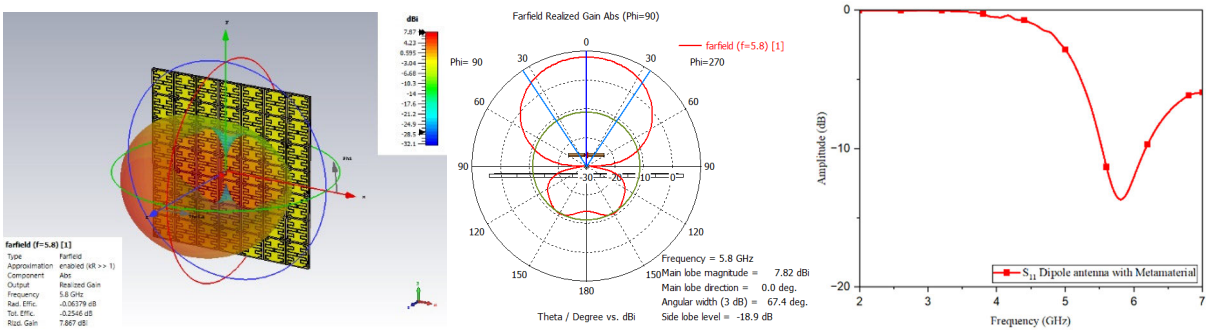


(c)

**FIGURE 18.** The simulated results of radiation pattern with gain and frequency response at (a) 1.8 GHz, (b) 3.7 GHz, and (c) 5.8 GHz.

space to simulate an air environment, and the signal at the input port excites the dipole antenna with the unit cell array.

The simulation results depicted in Fig. 18(a) indicate that transmission property occurs at the first resonant frequency of 1.8 GHz due to the positive permittivity and negative permeability at this frequency. With a gain of 5.49 dBi, a propagation direction of 0 degrees, a reflection coefficient ($S_{11}$) of less than −10 dB, and a bandwidth of 258 MHz at this frequency, electromagnetic wave transmission between the dipole antenna and the unit cell array is adequate. This material qualifies as a director at this frequency. The simulation results at the second-order resonance frequency of 3.7 GHz, as shown in Fig. 18(b), reveal that the unit cell array has reflection property because, at this frequency, positive permeability and negative permittivity produce reflectors with superior reflection properties compared to conventional materials. It has a reflection direction of 0 degrees, a reflection coefficient of less than −10 dB, and a bandwidth of 590 MHz. Additionally, it has a directional reflection that can increase antenna gain by 8.21 dBi. Consequently, the material exhibits a high reflection at this resonant frequency. At the third-order resonance frequency of 5.8 GHz, the unit cell array has the reflection property as same the property that occurred at the second-order resonance frequency, where there is a positive permeability and a negative permittivity, resulting in a reflection property that is stronger than that of conventional material reflectors and second-order resonance frequency. In addition, it possesses the gain of the antenna with the proposed unit cell array is 7.87 dBi, a direction of reflection at 0 degrees, a reflection coefficient ($S_{11}$) less than −10 dB, and a bandwidth of 661 MHz as illustrated in Fig. 18(c). The simulation results demonstrate

**TABLE 2. Dipole antenna dimensions.**

| Dipole parameters | Dimension (mm) | | |
|---|---|---|---|
| | $f$ = 1.8 GHz | $f$ = 3.7 GHz | $f$ = 5.8 GHz |
| $L_S$ | 32.50 | 14.5 | 9.5 |
| $L_T$ | 68.00 | 46.0 | 20.0 |
| $G$ | 3.00 | 2.2 | 1.00 |
| $A$ | 3.46 | 3.46 | 3.46 |
| $T$ | 0.46 | 0.46 | 0.46 |

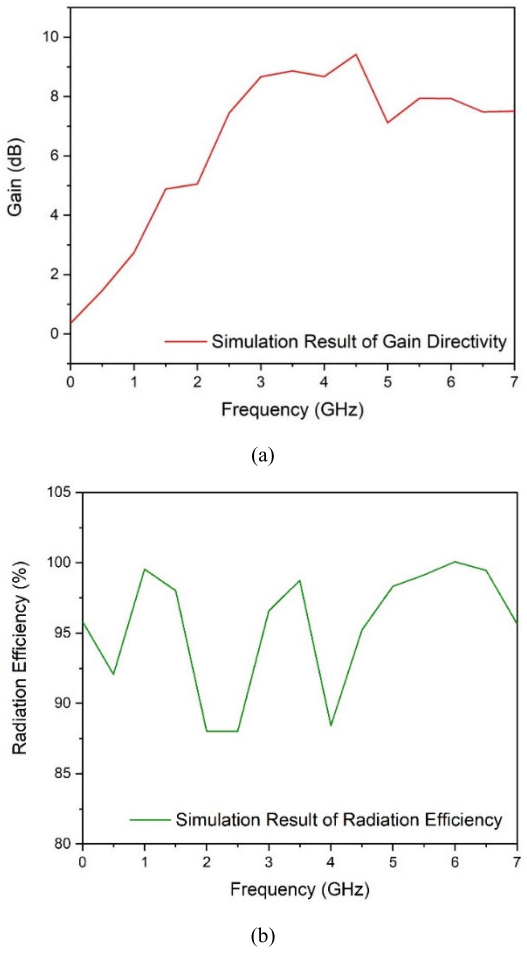


**FIGURE 19. The simulation results of the proposed unit cell array with dipole antenna: (a). Gain (b) radiation efficiency.**

that the property of the unit cell array has the same properties as that of a unit cell, including transmission and reflection properties, which can be controlled with the presented methodologies to achieve such properties.

Figs. 19 display the simulation results of the gain and radiation efficiency of the unit cell array including a dipole antenna, as presented in the present research. The figure in issue, Fig. 19(a), demonstrates that the proposed unit cell array antenna exhibits gains of 5.49 dBi, 8.21 dBi, and 7.82 dBi for the respective operating frequencies of 1.8 GHz, 3.7 GHz, and 5.8 GHz. Additionally, it can be shown from Figure 19(b) that the radiation efficiency of the unit cell under consideration, which incorporates a dipole, exceeds 87% throughout the whole frequency range of operation. In addition, the electric field will be evaluated and analyzed as shown in Figs. 20. At the first-order resonance frequency as depicted in Fig. 20(a), a large number of $E$-field values are generated on the transmission line and interdigital structures, but predominantly in the transmission line region, indicating that the transmission line is primarily responsible for the resonance at this frequency. Because the capacitive load in the interdigital region has a negligible effect on this frequency, the $E$-field in this region is smaller. Additionally, there are $E$-field intensity in the interdigital and transmission line ranges at second-order resonant frequency as illustrated in Fig. 20(b). However, the apparent electric field intensity was found to be greater in the interdigital region than in the transmission line region at this frequency. Therefore, this indicates that resonance at second-order frequency is primarily caused by capacitive load and can be controlled together with transmission line impedance difference using trisection step-impedance techniques. Fig. 20(c) shows the simulation result of the $E$-filed intensity at the third-order resonance frequency of 5.8 GHz. The $E$-field intensity is equivalent to the first-order resonance frequency, which corresponds to the same frequency range for the odd mode. The resonant frequency in this range is predominantly determined by the impedance difference on the transmission line, while the capacitive load has a negligible influence. Therefore, from the aforementioned simulation results it was found that the structure of the 7 × 7 unit cell array has a good resonant frequency response of 1.8 GHz, 3.7 GHz, and 5.8 GHz. It also has a dual-mode characteristic that can be applied as a director or reflector to increase the gain efficiency in conjunction with the antenna. The prototype fabrication and measurement will be presented in the next section.

## IV. MEASUREMENT RESULTS

The proposed 7 × 7 unit cell array or proposed metamaterial with the dipole antenna is presented in this part along with the manufacturing and measurement findings. The prototype of the proposed metamaterial, as outlined in the preceding section, will be fashioned using FR-4 printed circuit board with the dielectric constant ($\varepsilon_r$) of 4.4, the substrate thickness of 1.6 mm, the loss tangent (tan$\delta$) of 0.04, and the conductor thickness of 0.035 mm. The prototype metamaterial was fabricated utilizing an LPKF milling machine and possesses dimensions of 98 mm × 98 mm. Subsequently, each dipole antenna with a single frequency, which was previously designed through simulation, will be produced at the resonant frequencies of 1.8 GHz, 3.7 GHz, and 5.8 GHz. The fabrication of each prototype antenna will consist of the connection of a copper tube to a low-loss RG-45 cable, which will be fed by SMA-51. Furthermore, a balun circuit will be installed to transform impedance matching and compensate for the current between the unbalanced and balanced lines. Fig. 21(a) depicts the demonstration of the prototype metamaterial

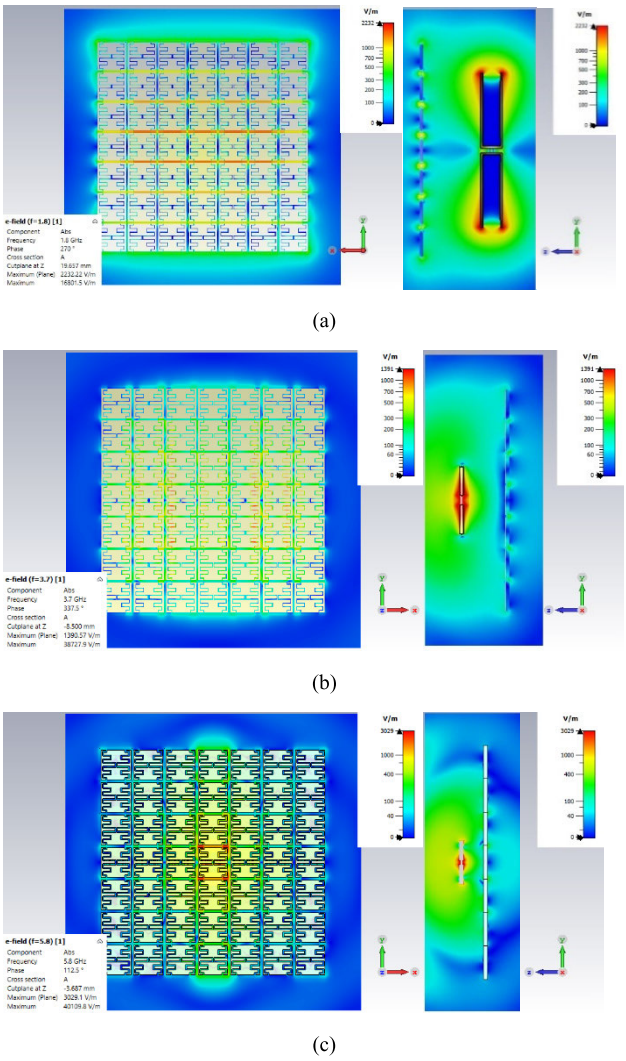


**FIGURE 20.** The E-field intensity's simulation results of the proposed unit cell array with dipole antenna: (a). director or reflector mode and (b) bound condition.

alongside the single-frequency dipole antenna. The properties of the metamaterial featuring the dipole antenna will be examined and evaluated within the confines of the anechoic chamber room, as depicted in Fig. 21(b). In the context of measurement installation, the proposed metamaterial will be positioned in front of the antenna at a frequency of 1.8 GHz to examine the transmission characteristics in director mode. Conversely, the proposed metamaterial will be positioned behind the antenna at frequencies of 3.7 GHz and 5.8 GHz to assess the reflection characteristics in reflector mode. At the resonant frequencies of 1.8 GHz, 3.7 GHz, and 5.8 GHz, the separation distances between the antenna and the metamaterial are 15.3 mm, 12.4 mm, and 7.6 mm, respectively. The magnitude of this distance is contingent upon the dimensional characteristics of the unit cell architecture. Given that the proposed structure is approximately $\lambda/8$ in size, it is imperative that the distance between the proposed metamaterial and the antenna be shorter than that of conventional materials to

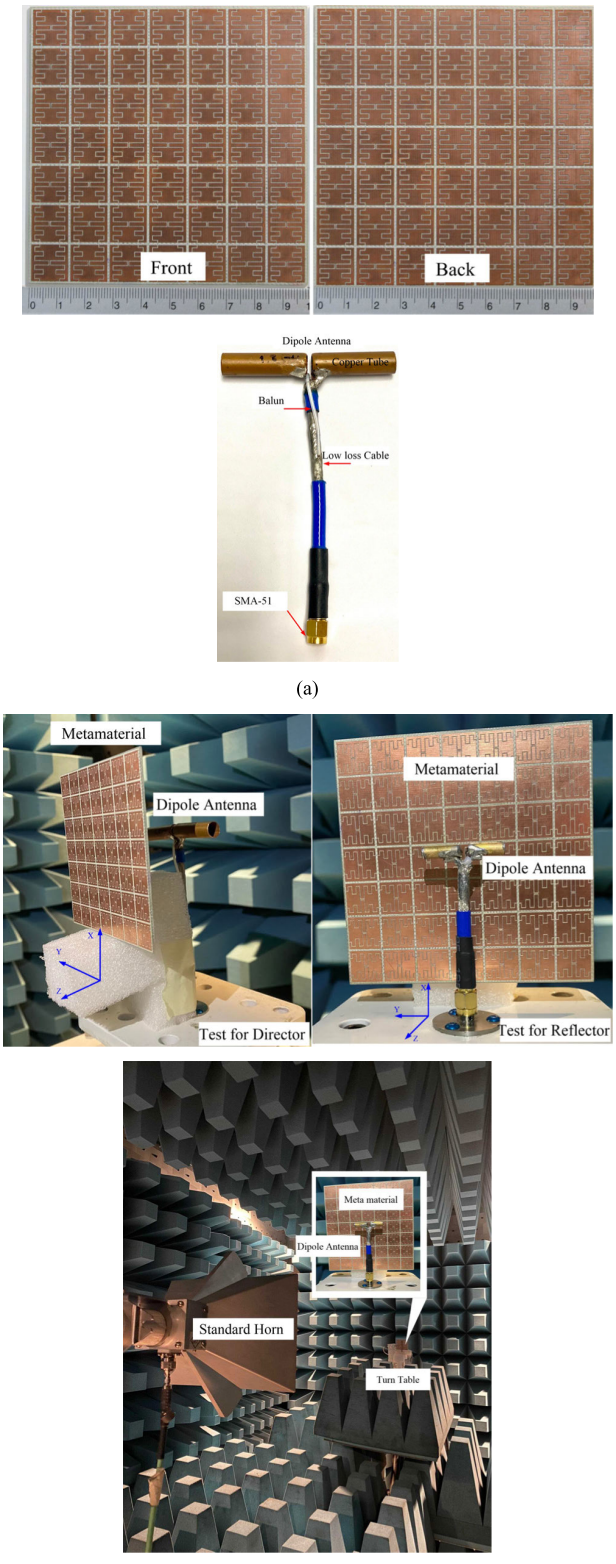


**FIGURE 21.** The prototype metamaterial with the antenna (a) configuration (b) the measurement installation in the anechoic chamber room.

ensure the in-phase alignment of the electromagnetic wave for optimal transmission or reflection effects. Figs. 22 depict

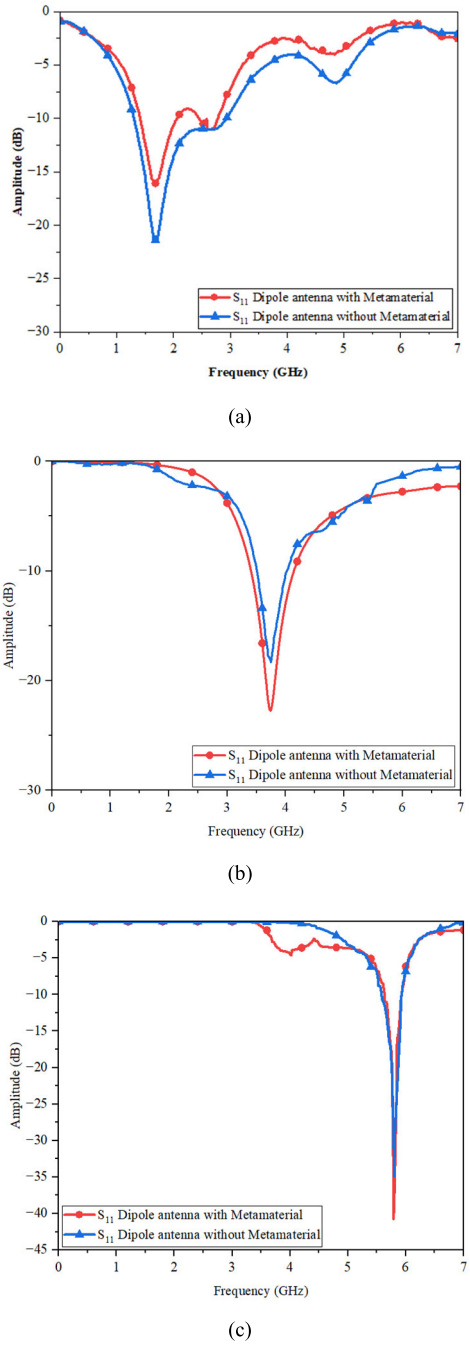


**FIGURE 22.** The comparison of measured return losses $|S_{11}|$ of the dipole antenna with the proposed metamaterial and without the proposed metamaterial at (a) 1.8 GHz, (b) 3.7GHz, and (c) 5.8 GHz.

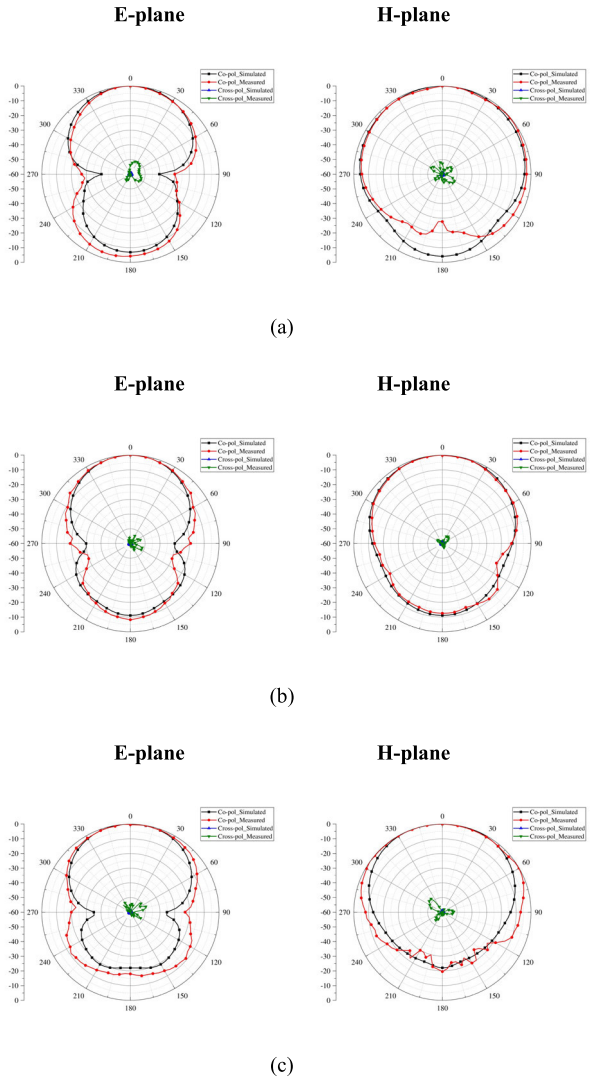


**FIGURE 23.** Measured radiation patterns in E-plane and H-plane of the metamaterial with the antenna at (a) 1.8 GHz, (b) 3.7 GHz, and (c) 5.8 GHz.

a comparison of the return loss $|S_{11}|$ between the simulated and measured results for the proposed metamaterial incorporated with the antenna. The obtained outcomes indicate that the metamaterial proposed in conjunction with the antenna yields a return loss of $|S_{11}| < -10$ dB across all resonant frequencies. The impedance bandwidths for different frequencies have been determined. At a frequency of 1.8 GHz, the impedance bandwidth is approximately 190 MHz, spanning 1.69 GHz to 1.88 GHz. At a frequency of 3.7 GHz, the impedance bandwidth is 520 MHz, covering from 3.47 GHz to 3.99 GHz. Lastly, at a frequency of 5.8 GHz, the impedance bandwidth is 115 MHz, ranging from 5.735 GHz to 5.85 GHz. The findings suggest that the simulated and measured outcomes correspond well and cover the operating frequency.

The simulated and measured radiation patterns of the metamaterial with the antenna at the resonance frequencies of 1.8 GHz, 3.7 GHz, and 5.8 GHz are shown in Fig. 23. The findings suggest a strong concurrence between the simulated outcomes and the measured data. At the resonant frequency of 1.8 GHz, it is evident that radiation patterns exhibit bidirectional characteristics in both $E$- and $H$-planes. The proposed metamaterial exhibits negative permeability and positive permittivity at a specific frequency, thereby possessing transmission characteristics. The specific characteristic is comprehensively explained in [22] and [23]. It demonstrates the capability to efficiently manipulate electromagnetic waves that are scattered within the metamaterial.

**TABLE 3. Performance comparison with reported single negative SNG ($\varepsilon < 0$ and/or $\mu < 0$) metamaterial resonators from the literature.**

| Reference Number | No. of bands (structure shaped) | Freq.(GHz) | Unit cell size ($mm^3$) | Overall size ($mm^3$) | No. of unit cell array | Measurement gain (dB) | Type of Applications |
|---|---|---|---|---|---|---|---|
| [3] | 1 (Square patch single cell) | 2.4, 3.7 and 5.1 | 3×3×1.59 | 3×3×1.59 | 1 | - | Load for antenna |
| [4] | 1 ( Slot square patch ) | 2.7 THz-5 THz | 19µm×19µm× 220 nm | 100µm ×115 µm ×220 nm | 5×6 | - | Absorber |
| [37] | 4 (C chape splitring resonator) | 0.9, 2.4, 3.5 and 5.5 | 5.8×5.8 ×1.6 | 76×42.5 ×1.6 | 13×8 | 1.89, 5.05, 6.74 and 5.98 | Increase gain of Antenna |
| [6] | 2 (Cross circular loop with Stub) | 9.85- 12 | 5×5×0.5 | 5×5×0.5 | 1 | - | Metamaterial Transmission |
| [8] | 1 (Snow flake shape) | 11.5, 13.5, 15.2 and 16.8 | 4.1×3.2×1 | 4.1×3.2×1 | 1 | - | Absorber |
| [38] | 1 (Triangular with array pin) | 3.5, 5.7 and 6.2 | 26×26×1.27 | 26×26×1.27 | 1 | 3.8 and 5.5 | Reflector |
| [12] | 1 (Spherical Spiral) | 0.155-0.199 and 0.139-0.181 | Radius 10.5 | 22×22×1.6 | 5×5 | - | Double negative material |
| [13] | 2 (MTM) | 8-12 | 15×15×0.8 | 120×120×0.508 | 15×15 | - | Absorber |
| [14] | 1 (LHM square spiral ) | 0.13-0.14 | 38 × 38 ×1.6 | 190 ×190×1.6 | 5×5 | - | Power transfer |
| [17] | 2 (Jerusarem with Interdigital) | 1.8 and 5.5 | 22.53×23.24×0.762 | 126×126×0.762 | 5×5 | 8.06 and 9.16 | Reflector |
| Metamaterial in proposed | 3 (ICPW with Meander line) | 1.8, 3.7 and 5.8 | 14×14×1.6 | 98×98×1.6 | 7×7 | 5.73 8.19 7.79 | Director and Reflector |

Moreover, it can arrange these waves into plane waves and subsequently emit them with a propagation direction of 0 degrees. This phenomenon results in an enhancement of the antenna's gain upon wave release, especially when utilized in combination with the director element. This allows the metamaterial to receive and promptly transmit electromagnetic waves from the antenna, resulting in a radiation pattern magnitude of the front lobe that is similar to that of the back lobe. In contrast, it can be observed that the radiation pattern in the $E$- and $H$-planes at the resonant frequencies of 3.7 GHz and 5.8 GHz exhibit a directional behavior. This can be attributed to the reflective properties of the metamaterial, which is characterized by a positive permeability and negative permittivity. The existence of a negative permittivity inside the metamaterial leads to an enhanced reflection index, thereby increasing the antenna gain. The observed enhancement may be ascribed to the metamaterial's capacity to align electromagnetic waves and efficiently accumulate their energy at a suitably elevated level before their subsequent reflection back to the antenna [22], [23]. When the reflection phase angle is equal to zero degrees, the radiated waves will exhibit a state of coherence with the antenna. The use of the suggested metamaterial leads to a reduction in the separation between the antenna and reflector, which is equivalent to less than one-fourth of the wavelength ($\lambda/4$). This outcome is a direct consequence of this specific characteristic.

However, the analysis of Figs. 23 reveals that the back lobe exhibits a significant increase in amplitude subsequent to the connection of the metamaterial. Metamaterials have the unique ability to function as both a director and a reflector due to their inherent characteristics. The initial resonant frequency of the metamaterial exhibits energy transmission characteristics as a result of its negative permeability and positive permittivity, leading to the predominant forward release of energy. Simultaneously, there exists a residual propagation of energy in the opposite direction. This phenomenon occurs due to the inherent limitation of the metamaterial in effectively transmitting the whole of the energy, resulting in the redirection of the energy emitted by the dipole antenna. Subsequently, while examining the second and third resonant frequencies, it was determined that the metamaterial exhibits energy reflection characteristics. This phenomenon may be attributed to the near-zero permeability and negative permittivity. Consequently, the placement of the metamaterial behind the antenna induces wave reflection in the frontal direction. Nevertheless, it is evident that the back lobe continues to manifest in the posterior aspect. This phenomenon occurs due to the fact that, while operating at these specific frequencies, the metamaterial exhibits a very negligible permeability, resulting in its capacity to transfer energy. Due to this rationale, it is observed that when a dipole antenna is positioned in front of a metamaterial, a certain amount of energy is able to traverse the metamaterial and propagate towards the rear. Consequently, it is not possible for all energy to be fully reflected. Nevertheless, a significant portion of the energy continues to be reflected in the direction facing the antenna, making metamaterials a viable option for their use as reflectors.

Furthermore, the levels of cross-polarization in both the $E$-plane and $H$-plane exhibit significant reduction across all resonant frequencies. Particularly, the simulated cross-polarization levels in both the $E$- plane and $H$-plane demonstrate values below −60 dB. This discrepancy is rather insignificant when compared to the observed data, as seen in Fig. 23. The proposed metamaterial has resulted in an antenna gain of 5.73 dBi, 8.19 dBi, and 7.79 dBi at the resonant frequencies of 1.8 GHz, 3.7 GHz, and 5.8 GHz, respectively. At all resonant frequencies, the proposed metamaterial ensures that the antenna's direction beam is fixed at 0 degrees. Based on the measurements presented in Figs 22 and 23, it is evident that the test outcomes exhibit a high degree of proximity to the simulated results. The metamaterial under consideration exhibits the characteristic of functioning as a director or reflector within the resonant frequency ranges of 1.8 GHz, 3.7 GHz, and 5.8 GHz. This property enables the material to transmit and reflect waves at the desired resonant frequencies to a greater extent than conventional materials. The unit cell structure of the metamaterial has been designed using the ICPW technique, which accounts for this enhanced functionality. Furthermore, the metamaterial structure that has been designed exhibits a significant enhancement in the antenna's gain within the resonant frequency range. Table 3 presents a comparative analysis between the proposed metamaterial with the antenna and the reference antennas. The device exhibits the capability of operating within a maximum of three distinct frequency bands and possesses a significant level of amplification.

## V. CONCLUSION

This research presents a novel approach for achieving multiband operation through the utilization of miniaturized metamaterial, specifically the dual-mode characteristic of director/reflector. The formation of the unit cell is achieved through the implementation of the interdigital coplanar waveguide (ICPW) methodology, in conjunction with the trisection step-impedance approach, which facilitates the resonance of the triple resonant frequency. The research utilized an interdigital coplanar waveguide (ICPW) approach that is based on CPW. The results indicated that augmenting the capacitive load linking the transmission line and the ground had a discernible impact. The utilization of the interdigital technique yields a phenomenon of slow waves on the transmission line, wherein the electrical length and physical length of the transmission line exhibit dissimilar magnitudes. This leads to a decrease in the size of the unit cell from $\lambda/2$ to $\lambda/8$ when considering fundamental frequency. In order to achieve resonance at the three designated frequencies, it is necessary to utilize a trisection step-impedance technique in conjunction with a capacitive load on the structure. This approach enhances impedance matching and ensures that resonance occurs precisely as required. As a result, the overall size of the structure's unit cell is 14 mm × 14 mm. Moreover, the manipulation of capacitive value within the interdigital range can regulate the resonant frequency, thereby enabling the attainment of the intended resonance frequency. The capacitive effect pertains to the displacement of all resonance frequencies from the fundamental frequency and exerts a notable influence on the shifts of the second resonance frequency. The utilization of this methodology enables the development of a diminutive ICPW elementary unit that exhibits the capability to react to an extensive spectrum of frequencies. Upon connecting the unit cell in a 7 × 7 configuration for utilization as a multiband director/reflector metamaterial, the resultant dimensions are notably diminutive, measuring 98 mm × 98 mm. The simulation findings revealed impedance matching below −10 dB across all resonant frequencies with antenna gains of 5.49 dBi, 8.21 dBi, and 7.87 dBi at 1.8 GHz (LTE), 3.7 GHz (WiMAX), and 5.8 GHz (Wi-Fi), respectively, when the proposed metamaterial was coupled to a single frequency dipole antenna. The proposed metamaterial in conjunction with the dipole antenna was evaluated in an anechoic chamber room to determine its efficacy. The results indicated an impedance matching of less than −10 dB. The target frequency band was covered by all resonant frequencies, which may have shifted differently from the simulation's predictions but remained within the designated frequency range. The research was targeted to evaluate the efficacy of the gain of the proposed metamaterial with the antenna by measuring its performance in the co-polarization of $E$-plane and $H$-plane at various frequencies. The findings demonstrate that the proposed metamaterial, when paired with the antenna, yields a gain of 5.73 dBi, 8.19 dBi, and 7.79 dBi in the co-polarization of $E$-plane at 1.8 GHz, 3.7 GHz, and 5.8 GHz, respectively. Similar to this, the proposed metamaterial's gain at 1.8 GHz, 3.7 GHz, and 5.8 GHz is 5.73 dBi, 8.19 dBi, and 7.82 dBi, respectively, with the antenna in the co-polarization of the $H$-plane. In the case of cross-polarization, the $E$- and $H$-planes both have extremely low antenna propagation. The findings indicate that there was a resemblance between the simulated outcomes and the measured outcomes. In summary, the proposed metamaterial represents a novel class of materials. The unit cell is intentionally scaled down in size to enable its use in smaller antennas. The metamaterial under consideration has the potential to serve as both a director and a reflector when used in combination with the antenna. Moreover, when used as a reflector in conjunction with an antenna, it exhibits the capability to reflect several frequencies simultaneously. Furthermore, the proposed metamaterial has the potential to further enhance the antenna's gain. It has the potential to be utilized across a variety of frequencies. The small size of the unit cell renders it appropriate for diverse applications, including deployment as a reflector for base stations, augmenting the transmission range in radar systems, amplifying microwave scans for GPR systems, and optimizing the efficiency of satellite antennas.

## REFERENCES

[1] C. Caloz and T. Itoh, *Electromagnetic Metamaterials: Transmission Line Theory and Microwave Applications*. New York, NY, USA: Wiley, 2006.

[2] J. K. Ji, G. H. Kim, and W. M. Seong, "A compact multiband antenna based on DNG ZOR for wireless mobile system," *IEEE Antennas Wireless Propag. Lett.*, vol. 8, pp. 920–923, 2009, doi: 10.1109/LAWP.2009.2028908.

[3] J. Zhu, M. A. Antoniades, and G. V. Eleftheriades, "A compact tri-band monopole antenna with single-cell metamaterial loading," *IEEE Trans. Antennas Propag.*, vol. 58, no. 4, pp. 1031–1038, Apr. 2010, doi: 10.1109/TAP.2010.2041317.

[4] Y. Ma, Q. Chen, J. Grant, S. C. Saha, A. Khalid, and D. R. S. Cumming, "A terahertz polarization insensitive dual band metamaterial absorber," *Opt. Lett.*, vol. 36, no. 6, p. 945, Mar. 2011, doi: 10.1364/OL.36.000945.

[5] D. K. Ntaikos, N. K. Bourgis, and T. V. Yioultsis, "Metamaterial-based electrically small multiband planar monopole antennas," *IEEE Antennas Wireless Propag. Lett.*, vol. 10, pp. 963–966, 2011, doi: 10.1109/LAWP.2011.2167309.

[6] J. Zhong, Y. Huang, G. Wen, H. Sun, O. Gordon, and W. Zhu, "Dual-band negative permittivity metamaterial based on cross circular loop resonator with shorting stubs," *IEEE Antennas Wireless Propag. Lett.*, vol. 11, pp. 803–806, 2012, doi: 10.1109/LAWP.2012.2208172.

[7] M. A. Antoniades and G. V. Eleftheriades, "Multiband compact printed dipole antennas using NRI-TL metamaterial loading," *IEEE Trans. Antennas Propag.*, vol. 60, no. 12, pp. 5613–5626, Dec. 2012, doi: 10.1109/TAP.2012.2211324.

[8] Y. Tian, G. Wen, and Y. Huang, "Multiband negative permittivity metamaterials and absorbers," *OptoElectronics*, vol. 2013, pp. 1–7, Jul. 2013, doi: 10.1155/2013/269170.

[9] H. Huang, Y. Liu, S. Zhang, and S. Gong, "Multiband metamaterial-loaded monopole antenna for WLAN/WiMAX applications," *IEEE Antennas Wireless Propag. Lett.*, vol. 14, pp. 662–665, 2015, doi: 10.1109/LAWP.2014.2376969.

[10] O. M. Khan, Z. U. Islam, Q. U. Islam, and F. A. Bhatti, "Multiband high-gain printed Yagi array using square spiral ring metamaterial structures for S-band applications," *IEEE Antennas Wireless Propag. Lett.*, vol. 13, pp. 1100–1103, 2014, doi: 10.1109/LAWP.2014.2329309.

[11] S. Jamilan, M. A. Antoniades, J. Nourinia, and M. N. Azarmanesh, "A compact multiband printed dipole antenna loaded with two unequal parallel NRI-TL metamaterial unit cells," *IEEE Trans. Antennas Propag.*, vol. 63, no. 9, pp. 4244–4250, Sep. 2015, doi: 10.1109/TAP.2015.2452952.

[12] K. L. Smith and R. S. Adams, "Spherical spiral metamaterial unit cell for negative permeability and negative permittivity," *IEEE Trans. Antennas Propag.*, vol. 66, no. 11, pp. 6425–6428, Nov. 2018, doi: 10.1109/TAP.2018.2864315.

[13] J. Tak, Y. Jin, and J. Choi, "A dual-band metamaterial microwave absorber," *Microw. Opt. Technol. Lett.*, vol. 58, no. 9, pp. 2052–2057, Sep. 2016, doi: 10.1002/mop.29977.

[14] H.-F. Huang and T. Li, "A minimized 2-D left-handed material spiral unit cell with rotation symmetry for midrange wireless power transfer," *IEEE Microw. Wireless Compon. Lett.*, vol. 27, no. 10, pp. 882–884, Oct. 2017, doi: 10.1109/LMWC.2017.2745485.

[15] Z. Qu, Y. Zhang, and B. Zhang, "Double square rings with different dimensions produce multiple absorption bands," *Appl. Opt.*, vol. 58, no. 1, pp. 152–157, Jan. 2019, doi: 10.1364/AO.58.000152.

[16] F. S. Jafari, M. Naderi, A. Hatami, and F. B. Zarrabi, "Microwave Jerusalem cross absorber by metamaterial split ring resonator load to obtain polarization independence with triple band application," *AEU, Int. J. Electron. Commun.*, vol. 101, pp. 138–144, Mar. 2019, doi: 10.1016/j.aeue.2019.02.002.

[17] W. Kamonsin, P. Krachodnok, P. Chomtong, and P. Akkaraekthalin, "Dual-band metamaterial based on Jerusalem cross structure with interdigital technique for LTE and WLAN systems," *IEEE Access*, vol. 8, pp. 21565–21572, 2020, doi: 10.1109/ACCESS.2020.2968563.

[18] R. Xu and Y.-S. Lin, "Reconfigurable multiband terahertz metamaterial using triple-cantilevers resonator array," *J. Microelectromech. Syst.*, vol. 29, no. 5, pp. 1167–1172, Oct. 2020, doi: 10.1109/JMEMS.2020.3007738.

[19] Y. Yuan, K. Zhang, B. Ratni, Q. Song, X. Ding, Q. Wu, S. N. Burokur, and P. Genevet, "Independent phase modulation for quadruplex polarization channels enabled by chirality-assisted geometric-phase metasurfaces," *Nature Commun.*, vol. 11, no. 1, Aug. 2020, Art. no. 4186.

[20] M. Hussain, W. A. Awan, M. S. Alzaidi, N. Hussain, E. M. Ali, and F. Falcone, "Metamaterials and their application in the performance enhancement of reconfigurable antennas: A review," *Micromachines*, vol. 14, no. 2, p. 349, Jan. 2023, doi: 10.3390/mi14020349.

[21] S. E. Mendhe and Y. P. Kosta, "Metamaterial properties and applications," *Int. J. Inf. Technol. Knowl. Manag.*, vol. 4, no. 1, pp. 85–89, 2011.

[22] N. Engheta and R. W. Ziolkowski, *Metamaterials: Physics and Engineering Explorations*. Hoboken, NJ, USA: Wiley, 2006.

[23] J. B. Pendry, A. J. Holden, D. J. Robbins, and W. J. Stewart, "Magnetism from conductors and enhanced nonlinear phenomena," *IEEE Trans. Microw. Theory Techn.*, vol. 47, no. 11, pp. 2075–2084, Nov. 1999.

[24] R. Marqués, F. Martín, and M. Sorolla, *Metamaterials With Negative Parameters: Theory, Design, and Microwave Applications*. Hoboken, NJ, USA: Wiley, 2008.

[25] M. Yan, J. Wang, H. Ma, M. Feng, Y. Pang, S. Qu, J. Zhang, and L. Zheng, "A tri-band, highly selective, bandpass FSS using cascaded multilayer loop arrays," *IEEE Trans. Antennas Propag.*, vol. 64, no. 5, pp. 2046–2049, May 2016, doi: 10.1109/TAP.2016.2536175.

[26] M. Mantash, A. Kesavan, and T. A. Denidni, "Beam-tilting endfire antenna using a single-layer FSS for 5G communication networks," *IEEE Antennas Wireless Propag. Lett.*, vol. 17, no. 1, pp. 29–33, Jan. 2018, doi: 10.1109/LAWP.2017.2772222.

[27] G. Das, A. Sharma, R. K. Gangwar, and M. S. Sharawi, "Performance improvement of multiband MIMO dielectric resonator antenna system with a partially reflecting surface," *IEEE Antennas Wireless Propag. Lett.*, vol. 18, no. 10, pp. 2105–2109, Oct. 2019, doi: 10.1109/LAWP.2019.2938004.

[28] L. Peng, C.-L. Ruan, and J. Xiong, "Compact EBG for multi-band applications," *IEEE Trans. Antennas Propag.*, vol. 60, no. 9, pp. 4440–4444, Sep. 2012, doi: 10.1109/TAP.2012.2207036.

[29] R. Pandey and D. K. Vishwakarma, "A meander line uniplanar EBG based multiband antenna using defected ground plane for WLAN and WiMAX applications," in *IEEE MTT-S Int. Microw. Symp. Dig.*, Dec. 2015, pp. 64–67, doi: 10.1109/IMaRC.2015.7411391.

[30] R. Dewan, M. K. A. Rahim, M. R. Hamid, and H. A. Majid, "Multiband reconfigurable antenna using EBG unit cells," in *Proc. IEEE APACE*, Dec. 2016, pp. 38–42, doi: 10.1109/APACE.2016.7916465.

[31] A. Yadav, S. Goyal, T. Agrawal, and R. P. Yadav, "Multiband antenna for Bluetooth/ZigBee/ Wi-Fi/WiMAX/WLAN/X-band applications: Partial ground with periodic structures and EBG," in *Proc. Int. Conf. Recent Adv. Innov. Eng. (ICRAIE)*, 2016, pp. 1–5.

[32] Q. Zheng, C. Guo, G. A. E. Vandenbosch, and J. Ding, "Low-profile circularly polarized array with gain enhancement and RCS reduction using polarization conversion EBG structures," *IEEE Trans. Antennas Propag.*, vol. 68, no. 3, pp. 2440–2445, Mar. 2020, doi: 10.1109/TAP.2019.2943693.

[33] Y. Cheon, J. Lee, and J. Lee, "Quad-band monopole antenna including LTE 700 MHz with magneto-dielectric material," *IEEE Antennas Wireless Propag. Lett.*, vol. 11, pp. 137–140, Jan. 2012, doi: 10.1109/LAWP.2012.2184517.

[34] C. Niamien, S. Collardey, A. Sharaiha, and K. Mahdjoubi, "Compact expressions for efficiency and bandwidth of patch antennas over lossy magneto-dielectric materials," *IEEE Antennas Wireless Propag. Lett.*, vol. 10, pp. 63–66, 2011, doi: 10.1109/LAWP.2011.2107493.

[35] Z.-G. Liu and Y.-X. Guo, "Compact low-profile dual band metamaterial antenna for body centric communications," *IEEE Antennas Wireless Propag. Lett.*, vol. 14, pp. 863–866, 2015.

[36] M. S. Soudi and H. M. Elkamchouchi, "A proposed multi-band metamaterial antenna based on a circular air slotted sievenpipper mushroom unit cell," in *Proc. IEEE Middle East Conf. Antennas Propag. (MECAP)*, Oct. 2010, pp. 1–7, doi: 10.1109/MECAP.2010.5724183.

[37] S. S. Al-Bawri, M. S. Islam, H. Y. Wong, M. F. Jamlos, A. Narbudowicz, M. Jusoh, T. Sabapathy, and M. T. Islam, "Metamaterial cell-based superstrate towards bandwidth and gain enhancement of quad-band CPW-fed antenna for wireless applications," *Sensors*, vol. 20, Jan. 2020, Art. no. 457, doi: 10.3390/s20020457.

[38] T. Wang, X. Wang, R. Wang, R. Xie, D. Chen, and S. Zhu, "Gain-enhanced antenna with metamaterial structure and pin array reflector for WiMAX and WLAN applications," *Microw. J.*, vol. 62, no. 8, pp. 134–142, Aug. 2019.

[39] J. Coonrod, "Comparing microstrip and CPW performance," *Microw. J.*, vol. 55, no. 7, pp. 74–82, 2012.

[40] P. Jirasakulporn, P. Chomtong, K. Bandudej, and P. Akkaraekthalin, "A compact triple band EBG using interdigital coplanar waveguide structure for antenna gain enhancement," *Int. J. Antennas Propag.*, vol. 2020, pp. 1–18, Dec. 2020, doi: 10.1155/2020/2856807.

[41] X. M. Lin and Q. X. Chu, "Design of triple-band bandpass filter using TRN-section stepped-impedance resonators," in *Proc. ICMMT*, Guilin, China, Apr. 2007, pp. 1–3, doi: 10.1109/ICMMT.2007.381479.
[42] Y.-C. Chen, Y.-H. Hsieh, C.-H. Lee, and C.-I. G. Hsu, "Tri-band microstrip BPF design using tri-section SIRs," in *Proc. IEEE Antennas Propag. Soc. Int. Symp.*, Jun. 2007, pp. 3113–3116, doi: 10.1109/APS.2007.4396195.
[43] F. Xu, L. Li, K. Wu, S. Delprat, and M. Chaker, "Parameter extraction of interdigital slow-wave coplanar waveguide circuits using finite difference frequency domain algorithm," *Int. J. RF Microw. Comput.-Aided Eng.*, vol. 18, no. 3, pp. 250–259, 2008, doi: 10.1002/mmce.20284.
[44] F. Xu, X. Liu, H. Guo, Y. Wang, and L. Mao, "A compact dual-mode BPF base on interdigital structure," in *Proc. IEEE ICMMT*, May 2010, pp. 1595–1597, doi: 10.1109/ICMMT.2010.5524850.
[45] R. S. Beeresha, A. M. Khan, and R. H. V. Manjunath, "Design and optimization of interdigital capacitor," *Int. J. Res. Eng. Technol.*, vol. 5, Special no. 21, pp. 73–78, Nov. 2016, doi: 10.15623/ijret.2016.0533016.
[46] S. Meesomklin, P. Chomtong, and P. Akkaraekthalin, "A compact multiband BPF using step-impedance resonators with interdigital capacitors," *Radioengineering*, vol. 25, no. 2, pp. 258–267, Apr. 2016, doi: 10.13164/re.2016.0258.
[47] W. Cheng, L. Li, G. Liu, Y. Xiao, Z.-Y. Wang, and J.-X. Yang, "An interdigital capacitor loaded slot antenna with compact size," *Prog. Electromagn. Res. Lett.*, vol. 64, pp. 15–19, 2016.

**P. CHOMTONG** (Member, IEEE) received the M.Eng. and Ph.D. degrees in electrical engineering from the King Mongkut's University of Technology North Bangkok (KMUTNB), Thailand, in 2006 and 2011, respectively. In 2012, he joined the Department of Teacher Training in Electrical Engineering, KMUTNB, as an Instructor. His current research interests include passive and active microwave circuits, wideband and multiband antennas, and telecommunication systems.

**P. KRACHODNOK** (Member, IEEE) received the M.Eng. degree in electrical engineering from Chulalongkorn University (CU), Thailand, in 2001, and the Ph.D. degree in telecommunication engineering from the Suranaree University of Technology (SUT), Thailand, in 2008. Since 2001, she has been with the School of Telecommunication Engineering, SUT. She has experience and an expert in electromagnetic theory, microwave engineering, and antenna engineering.

**C. MAHATTHANAJATUPHAT** (Member, IEEE) received the M.Eng. degree from the University of Applied Sciences Rosenheim, Germany, in 2003, and the Ph.D. degree from the King Mongkut's University of Technology North Bangkok (KMUTNB), Thailand, in 2009. In 2017, he was appointed as a Lecturer (Associate Professor) with the Department of Electrical Engineering, KMUTNB. His research interests include the designing of small antennas using the fractal geometry and digital signal processing for communication applications.

**N. SOMJIT** (Senior Member, IEEE) received the Dipl.-Ing. (M.Sc.) degree from the Dresden University of Technology, Dresden, Germany, in 2005, and the Ph.D. degree from the KTH Royal Institute of Technology, Stockholm, Sweden, in 2012. Then, he returned to TU Dresden to lead the Research Team in Microsensors and MEMS ICs for the Chair for Circuit Design and Network Theory. In 2013, he was appointed as a Lecturer (Assistant Professor) with the School of Electronic and Electrical Engineering, University of Leeds, Leeds, U.K., where he is currently an Associate Professor. Since 2022, he has been leading a Research Team as an Adjunct Faculty Member with the Micro and Nanosystems Department, KTH Royal Institute of Technology. His research interests include integrated smart high-frequency components, sustainable micro and nanosystems, and low-cost microfabrication processes. He was appointed as a member of the Engineering, Physical and Space Science Research Panel, British Council, in 2014. He was a recipient of the Best Paper Award (EuMIC Prize) from the European Microwave Week, in 2009. He was awarded the Graduate Fellowship from the IEEE Microwave Theory and Techniques Society (MTT-S), in 2010 and 2011, and the IEEE Doctoral Research Award from the IEEE Antennas and Propagation Society, in 2012. In 2016, he was the Chair of the Student Design Competition for the European Microwave Week. In 2018, he was appointed as an Associate Editor of *IET Electronics Letters*.

**P. AKKARAEKTHALIN** (Member, IEEE) received the B.Eng. and M.Eng. degrees in electrical engineering from the King Mongkut's University of Technology North Bangkok (KMUTNB), Thailand, in 1986 and 1990, respectively, and the Ph.D. degree from the University of Delaware, Newark, USA, in 1998. From 1986 to 1988, he was with the Microtek Laboratory, Thailand. In 1988, he joined the Department of Electrical Engineering, KMUTNB. He is currently the Head of the Senior Research Scholar Project of Thailand Research Fund (TRF). His current research interests include passive and active microwave circuits, wideband and multiband antennas, and telecommunication systems. He is a member of IEICE, Japan, and ECTI, Thailand. He was the Chairperson of the IEEE MTT/AP/ED Thailand Joint Chapter, from 2007 to 2008, and the President of the ECTI Association, from 2014 to 2015.